Synthesis and Modification of Zinc Oxide Nanoparticles for Antimicrobial Activities and UV light Protection

By

Prof. Abebe Belay

A Final Research Report Submitted to Adama Science and Technology University

Adama, Ethiopia
December, 2022

Acknowledgments

The author would like to acknowledge Adama Science and Technology University and for financial support. I also like to appreciate the National Institute of Technology, Physics Department, Warangal, India and Department of Material Sciences and Engineering of ASTU for allowing us to use the XRD for characterization of our samples. I also would like to acknowledge Pusan National University, Department of Nanoscience and Nanotechnology, South Korea for allowing us to use DLS, Fluorescence spectroscopy, and TEM Instruments. Also Addis Ababa Science and Technology University for allowing us to use SEM.

Abstract

In this research the effects of temperature and polyvinyl Alcohol (PVA) concentrations on the structural and optical properties of zinc oxide nanoparticles were investigated using a simple and cost effective sol-gel method. The XRD and SEM images of ZnO NPs indicated increment in the particle size as temperature and PVA concentration increased. Also the antimicrobial activity of zinc oxide (ZnO) nanoparticles (NPs) synthesized by different chemical, thermal and green routes were systematically investigated with an aim to determine which method yields the most efficient antimicrobial property. The experimental results showed that the antimicrobial activity of ZnO NPs increased with decreasing size of the crystal. Interestingly, the antimicrobial activity of ZnO NPs synthesized using green route was more effective than the chemical or thermal route. The binding of ZnO NPs with caffeic acid (CFA) were also investigated by fluorescence quenching, UV-Vis, FTIR, TEM and DLS under human physiological conditions. The study results indicated the fluorescence quenching between ZnO NPs and CFA were rationalized in terms of static quenching mechanism or the formation of non-fluorescent CFA-ZnO. From fluorescence quenching spectral analysis the quenching constant (k_{sv}), quenching rate constant (k_q), binding constant (K_a), number of binding site (n), thermodynamic properties, and conformational changes of the interaction were determined. ZnO NPs were synthesized at different temperatures and reaction media of water (S-1) and 1, 2-ethanediol (S-2) using precipitation and *in situ* methods on the surface of cotton fabric for UV light protection. The UV protection ability of ZnO NPs coated on textiles was investigated using UV-Vis spectroscopy by measuring the ultraviolet protection factor (UPF) in the ranges of 280-400 nm. Higher values of UPF were obtained for ZnO NPs prepared using an *in situ* method. The UPF value obtained by this method was found to be 320 which demonstrate its excellent ability to block UV radiation.

Key words: ZnO, Characterizations, Antimicrobials, UPF, Quenching

Table of Contents

List of figures

Lists of Tables

Lists of Abbreviations

Caffeine Acid	CFA
Colony Forming Unit	CFU
Dynamic Light Scattering	DLS
Fourier Transform Infra-Red	FTIR
Full Width at Half Maxima	FWHM
Mean Hydrodynamic Diameter	MHD
Minimum Inhibatory Concentration	MIC
Nanoparticles	NPs
Near Band Edge	NBE
Polyvinyl Alcohol	PVA
Reactive Oxygen Species	ROS
Scanning Electron Microscopy	SEM
Transmission Electron Microscopy	TEM
Tryptic Soy Agar	TSA
Ultraviolet A	UVA
Ultraviolet B	UVB
Ultraviolet Protection Factor	UPF
X-Ray Diffraction	XRD
Zinc Oxide	ZnO

1. Introduction

1.1. Background

Among several metal oxide nanoparticles (NPs), zinc oxide (ZnO) NPs classified as a semiconductor having own vast area of applications (Zhong & Matijević, 1996). It has tremendous scientific and technological interest, having a direct wide band gap (3.37 eV), large exciton-banding energy (60 meV), and high thermal and mechanical stability at room temperature which makes it attractive potential for various industrial and medical applications (Bahnemann et al., 1987). Synthesis of ZnO NPs by controlling particle size/distribution, composition, aggregation/agglomeration, shape, surface area, surface charge and surface chemistry can widely be used in many industrial areas such as Rubber, textile, ceramic and cosmetic industries. Furthermore, it can also useful to prepare various devices such as solar cells, lasers, UV light-emitting devices, gas and biological sensors, transistors (Kolodziejczak-Radzimska & Jesionowski, 2014).

Recent study report indicated the major global productions of zinc oxides are consumed by rubber industry to manufacture various different cross-linked products. The thermal conductivity of pure silicone rubber is relatively low; however it can be improved by adding certain thermal conductivity filters such as ZnO NPs without changing the electric resistance, thus ZnO promising candidate as high-performance engineering materials (Das et al., 2011).

ZnO NPs has also great potential applications in cosmetic industries largely due to increases in surface area to volume ratio, quantum effects which can affect the chemical reactivity and other physical and chemical properties. Previous studies indicated cosmetic industries use NPs which generate products with improved texture, more vibrant color and greater skin penetration (Cross et al., 2007 ; Uddin et al., 2008). Due to its inherent ability to absorb UV irradiation and optical transparency, the distinctive properties of Zinc oxide nanoparticles are of particular interest to the skin care industry (Carlotti et al., 2004; Newman et al., 2009). The zinc oxide nanoparticles also have useful applications in textile industry, since ZnO coatings are more air permeable and efficient UV-blockers compared with bulk counterparts. Its nanostructures have become very attractive as UV-protective textile coating and to impart self-cleaning and water repellent (Becheri et al., 2008; Xin et al., 2004; Kathirvelu et al., 2009).

It is universally known that zinc oxide nanoparticles (ZnO-NPs) have antibacterial activities and inhibit the growth of microorganisms by penetrating into the cell membrane.

Oxidative stress damages lipids, carbohydrates, proteins, and DNA (Siddiqi et al., 2018) of microorganisms. Hence, Zinc oxide nanoparticles (ZnO-NPs) have been used as an antibacterial substance against Salmonella typhi and S. aureus in vitro. Among all metal oxide nanoparticles studied against microorganisms, zinc oxide nanoparticles by far exhibited the highest toxicity against microorganisms

The other research studies indicated the modification of zinc oxide using organic compounds such as carboxylic acids (such as stearic, tartaric, maleic, propanoic *etc*) which makes it possible to introduce characteristic groups onto the surface of the ZnO and to alter its physicochemical properties, to increase the compatibility of ZnO with organic matrix, to reduce aggregation of particles and enhance long term stability in organic materials. Studies of zinc oxide modified with carboxylic acids (wet modification) have shown that they do not significantly affect the morphological/dispersive or porous properties of zinc oxide. An apparently promising method is modification *in situ,* which causes a significant increase in the surface area of the zinc oxide). In this regards the modification of ZnO NPs especially using biologically active compound of coffee beans not yet investigated.

Synthesis of nanoparticles having different shape and size *via* easy synthetic routes is the main issue in nanoparticle growth. For the past decade, scientists have been involved in the development of new synthetic routes enabling the precise control of the morphology and size of the nanoparticles. The zinc oxide occurs in a very rich variety of structures and offers a wide range of properties. The variety of methods for ZnO production, such as thermal techniques, hydrothermal synthesis, the sol-gel process, precipitation green methods processes, and makes it possible to obtain products with particles differing in shape, size and spatial structure. In this research, chemical, sol-gel, green and thermal methods were applied which is the most popular methods due to their low cost, reliability, and environmentally friendly synthetic routes, and this method provides rigorous control of the size and shape of the nanoparticles. In addition, the synthesized NPs are applied for antimicrobial activities, and incorporated on cotton textiles for UV light protection and antimicrobial activities. Also the binding of ZnO NPs bioactive compounds of coffee beans were investigated.

Most countries like America, European, China and South Korea are currently uses NPs for technological and medical applications widely, on the other hand, the applications of these technologies in Africa, in general and particularly in Ethiopia are rarely available.

So this research proposal expected to fill the research gaps existed in the country with the following general and specific objectives.

1.2. Objectives

1.3. General Objectives

The general objectives of this research is to synthesis and modify ZnO NPs for Antimicrobial activities and UV light protection

1.4. Specific Objectives

The specific objectives of the research is to

- Determine the effects of calcinations temperatures and concentrations of PVA on morphology, structure, sizes and optical properties of ZnO NPs
- Synthesize different size and shape of ZnO NPs using sol-gel, thermal decomposition, precipitation, green methods and apply for antimicrobial activities
- Synthesize the different size and shape of ZnO NPs using sol-gel, thermal decomposition, precipitation, green methods, *in situ* methods for UV light protection in cotton textiles
- Identify the binding mechanism ZnO with caffeic acid
- Modify the surface of ZnO NPs using caffeic acid
- Characterze the synthesis ZnO NPs using XRD, SEM, TEM, UV-Vis absorption, (DLS), and fluoresence spectroscopy techniques

2. Literature Review

2.1. Nanoparticles

Nanoparticles (NPs) are known as controlled or manipulated particles at the atomic level (1–100 nm) (Sirelkhatim et al., 2015). Nanoparticles are is a special group of materials with unique features and extensive applications in diverse fields. Studying these particular features has always been of great interest to many scientists. Nanoparticles display unique properties in comparison with their bulk size counterparts. A large number of materials that were considered to be safe develop toxicity at nano-size ranges which are mainly related to the increased specific surface area and high reactivity of nano-sized materials (Emami-karvani & Chehrazi, 2011).

2.2. Nanoscience and Nanotechnology

Nanotechnology is the art and science of manipulating matter at the nanoscale to create new and unique materials and products with enormous potential to change society (Upadhyaya et al., 2018). This technology is capable of providing miscellaneous novel applications that range from innovative fabric compounds, food processing, and agricultural production to sophisticated medicinal techniques. It is considered as the synthesis, characterization, and exploration of materials in the nanometer region (1–100 nm) (Sirelkhatim et al., 2015). Likewise, Nanotechnology is a scientific and engineering technology conducted at the Nano-scale, such as in the fields of compound fabric manufacturing, food processing, agricultural processing, and engineering, as well as in medical and medicinal applications (Hoseinzadeh et al., 2017).

Nanotechnology is the manipulation or self-assembly of individual atoms, molecules, or molecular clusters into structures to create materials devices with new or vastly different properties (Rl et al., 2019). Nanotechnology can be understood as a technology of design, fabrication, and applications of nanostructures and nanomaterials, as well as a fundamental understanding of the physical properties and phenomena of nanomaterials and nanostructures (D. Ahmed et al., 2015).

2.3. Fundamental properties of Zinc Oxide nanoparticles (ZnO-NPs)

Zinc oxide is an inorganic compound that occurs naturally as a mineral zincite or is chemically synthesized. It is an n-type semiconductor with a direct bandgap of 3.37 eV

(368 nm) and large exciton binding energy at room temperature of 60 meV is one of the most common materials because it has outstanding physical and chemical stability, low cost, high oxidizing power, high exciton binding energy, high transparency, high thermal stability, high biocompatibility. It has been widely used for optical, electrical, optoelectronic, catalytic, and photochemical properties, including optical waveguides and transparent conducting coatings. which makes it a suitable material for colossal applications such as flat panel displays (Sa-nguanprang et al., 2019) (Phuruangrat et al., 2014).

2.3.1. Crystal structure of Zinc Oxide nanoparticles (ZnO-NPs)

At room temperature and ambient pressure, Zinc Oxide nanoparticles (ZnO-NPs) have three different structures, namely the hexagonal wurtzite, zinc blende, and rock salt structures. Among, the most common structure of Zinc Oxide nanoparticles (ZnO-NPs) is the wurtzite crystal structure. The crystalline ZnO has a wurtzite structure that has a hexagonal unit cell with two lattice parameters of ‘a’ and ‘c’ and belongs to the space group of C^4_{6v} or P63mc. The lattice parameters of the hexagonal unit cells mostly range from 0.32475 to 0.32501 nm for ‘a’ and from 0.52042 to 0.52075 nm for ‘c’. The structure of ZnO can be simply described as several alternating planes composed of tetrahedrally coordinated O^{2-} and Zn^{2+} ions, stacked alternately along the c-axis. . In the wurtzite structure, each zinc ion is surrounded by four oxygen ions which are arranged in tetrahedral coordination, and alternatively each oxygen ion is surrounded by four zinc ions that are tetrahedrally coordinated along the c-axis. The tetrahedral arrangement of the zinc and oxygen ions gives rise to a non-centrosymmetric crystal structure of ZnO, consisting of two sub-lattices of zinc and oxygen atoms penetrating each other to form a hexagonal close-packed structure. When the bonds along the c-direction are from cation (Zn) to anion (O) the polarity is referred to be as Zn polarity.

In addition to polar surfaces, it also has non-polar surfaces. The four most common faces of wurtzite ZnO are the polar Zn-terminated (0001) and O-terminated ($000\bar{1}$) faces (c-axis oriented), and the ($2\bar{1}\bar{1}0$) (a-axis) and ($01\bar{1}0$) faces that contain an equal number of Zn and O atoms. The ($2\bar{1}\bar{1}0$) (a-axis) and ($01\bar{1}0$) faces are non-polar surfaces and have lower energy than the {0001} facets. Furthermore, the polar surfaces and the ($01\bar{1}0$) surfaces are found to be stable; however, the ($2\bar{1}\bar{1}0$) face is less stable and generally has a higher level of surface roughness than its counterparts. It has been observed that the origination of various shapes of the ZnO crystals is due to the relative growth rates of different crystal facets and differences in the growth rates of different crystal planes (Hahn, 2011) (Z. L. Wang, 2004)(Stefaniuk et al., 2018).

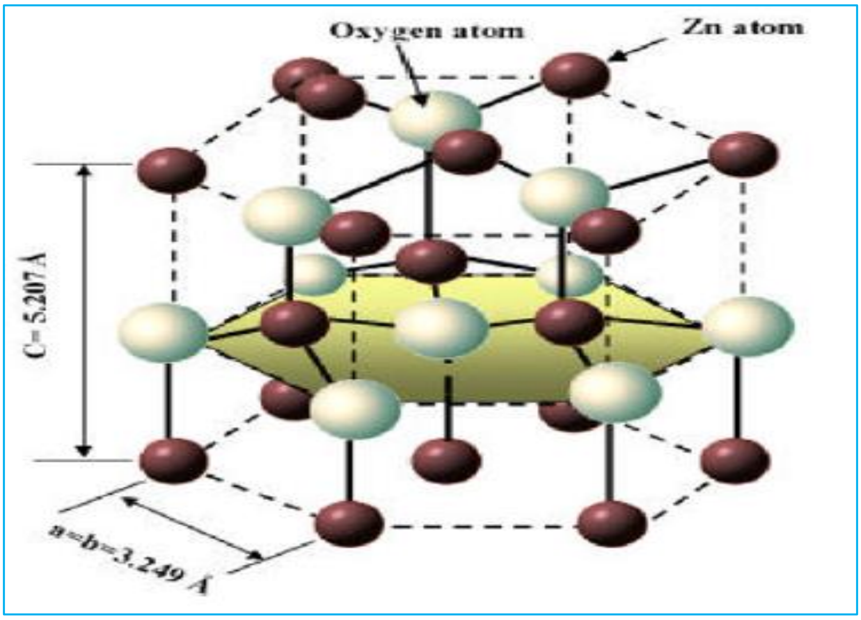

Figure 2.1: The hexagonal wurtzite structure model of ZnO. The tetrahedral coordination of Zn-O is shown. O atoms are shown as larger white spheres while the Zn atoms are smaller brown spheres (Hahn, 2011).

The crystal structures were investigated by XRD (x-ray diffraction) which is based on Wulf-Bragg's law presented in Eq (2.1). According to Bragg's law (Gadalla et al., 2018)

$$n\lambda = 2d\sin\theta \tag{2.1}$$

Where n is the order of diffraction (usually n = 1), λ is the X-ray wavelength and d is the spacing between planes of given Miller indices h, k, and l.

The plane spacing d to the lattice parameters ('a' and 'c') for the wurtzite hexagonal structure of ZnO can be calculated from (Karthikeyan et al., 2019).

$$\frac{1}{d^2_{hkl}} = \frac{4}{3}\left(\frac{h^2 + hk + k^2}{a^2} + \frac{l^2}{c^2}\right) \tag{2.2}$$

with the first order approximation (n = 1) Eq (2.2) above can be re written as Eq (2.3)(Devi & Velu, 2016b).

$$\sin^2\theta = \frac{\lambda^2}{4}\left(\frac{4}{3}\left(\frac{h^2 + hk + k^2}{a^2}\right) + \frac{l^2}{c^2}\right) \tag{2.3}$$

In the case of the wurtzite phase, the lattice parameters are calculated by using the formula Eqs (2.4-2.5) (Pradeev Raj et al., 2017).

$$a = \frac{\lambda}{\sqrt{3}\sin\theta_{100}} \tag{2.4}$$

$$c = \frac{\lambda}{\sin\theta_{002}} \tag{2.5}$$

Another method to authenticate the presence of dopant concentration is to estimate the presence of the bond length (L). The bond lengths are calculated using the relation of Eq(2.6) (Vijayaprasath et al., 2016).

$$L = \sqrt{\left(\frac{a^2}{3} + \left(\frac{1}{2} - u\right)^2 c^2\right)} \tag{2.6}$$

The positional parameter in the wurtzite structure and is determined by the amount by which each atom gets displaced for the ‘c’ axis given by Eq (2.7) (Raj et al., 2016).

$$u = \frac{a^2}{3c^2} + \frac{1}{4} \tag{2.7}$$

The average crystallite sizes of the synthesized samples were calculated from XRD spectra using Debye-Scherrer’s equation Eq (2.8)(Badreddine et al., 2018).

$$D = \frac{K\lambda}{\beta_{hkl}\cos\theta} \tag{2.8}$$

Where D is the average crystallite size of the particle, λ is the incident X-ray wavelength, β is the angular peak width at half maximum in radians, and θ is Bragg’s diffraction angle.

The dislocation density, δ is a measure of the number of defects and vacancies in the crystal, which can be determined from the crystallite size (D) using the relation in Eq (2.9) (Badreddine et al., 2018).

$$\delta = D^{-2} \tag{2.9}$$

The lattice expansion is quantified by the measurement of micro-strain which is given by Eq (2.10) (Choudhary, 2020).

$$\varepsilon = \frac{\beta \cos\theta}{4} \tag{2.10}$$

The unit cell volumes (V) for the hexagonal system were found from Eq (2.11) (Karthikeyan et al., 2019).

$$V = \frac{\sqrt{3}a^2 c}{2} = 0.866a^2 c \tag{2.11}$$

Atomic packing fraction has been calculated using the formula Eq (2.12) (Kumar et al., 2016).

$$APF = \frac{2\pi a}{3\sqrt{3}c} \tag{2.12}$$

2.3.2. Physical properties and parameters of Zinc Oxide nanoparticles (ZnO-NPs)

Nanotechnology applications are greatly depending on the fundamental properties of the nanomaterial. Therefore, knowing the fundamental physical properties of ZnO is crucial to the rational design of functional devices. It should be noted that as the dimension of the semiconductor materials shrinks down to nanometer scale, some of their physical properties change due to "quantum size effects". The physical parameters of the hexagonal wurtzite ZnO are summarized in Table 2.1.

Table 2.1: The basic physical properties of Zinc Oxide nanoparticles (ZnO-NPs) in wurtzite structure (Lu et al., 2005).

Property		Value
Lattice constants at (300K)	a	0.324 95 nm
	c	0.520 69 nm
	$\frac{c}{a}$	1.602 (ideal hexagonal structure shows 1.633)
	u	0.345
Density		5.606 gcm^{-3}
Stable phase at 300 K		Wurtzite
Melting point		1975 ℃
Linear expansion coefficient (/℃)		a: 6.5 × 10^{-6}

	c: 3.0×10^{-6}
Static dielectric constant	8.656
Refractive index	2.008, 2.029
Energy gap (300 K)	3.4 eV (direct band gap)
Exciton binding energy	60.0 meV
Magnetic susceptibility(χ)	$-27.2x10^{-6}\ cm^{3}mole^{-1}$
Electron effective mass	0.24
Hole effective mass	0.59
Bulk hardness, H (GPa)	5.0 ± 0.1
Electron mobility (T = 300 K) for low n-type conductivity	200 $cm^{2}V^{-1}s^{-1}$
Hole mobility (T = 300 K) for low n-type conductivity	5-50 $cm^{2}V^{-1}s^{-1}$

2.3.3. Optical properties of Zinc Oxide nanoparticles (ZnO -NPs)

The photo luminescent property of Zinc Oxide nanoparticles (ZnO-NPs) excited by UV radiation is usually exhibited by two prominent broad bands. The first band is located at 380nm in the Ultra Violet emission and is related to the band to band transition, known as near band edge emission (NBE) (Vijayaprasath et al., 2018), the second band is located in the visible region (450-800nm) and it is attributed to the deep-level emission (DLE). . It is well known that the visible emission of ZnO is due to the radiative recombination of a photo generated hole with an electron occupying the oxygen vacancy. The well-known defects in ZnO are oxygen vacancies (V_o), oxygen interstitials (O_i), oxygen antisites (Zn_O), zinc vacancies (V_{zn}), zinc interstitials (Zn_i) and zinc antisites (O_{Zn}). Visible light emission is a result of electron-hole recombination taking place at defect states (Ntwaeaborwa et al., 2017).

The UV emission is due to the near band–edge (NBE) emission of ZnO, which generates from the recombination of exciton-exciton through collision process. The emission in the visible range is referred to as a green emission, which is the emission outcome from the radiative recombination of a photo-generated hole with an electron occupying the oxygen vacancy. This green emission is due to the defects i.e. oxygen vacancy, zinc vacancy, oxygen interstitial, zinc interstitial.

2.4. Routes of synthesizing Zinc oxide nanoparticles

Two main approaches are used in synthesis of ZnO. The bottom up synthesis carries out by forming Zinc Oxide nanoparticles relatively from simpler substance. The approach also called building up approach. The sol-gel, green synthesis and biochemical synthesis are example of bottom up synthesis method and the top down synthesis method involves by starting with large molecule then decompose into smaller units. Examples of top down methods are grinding (milling), physical vapor deposition and decomposition techniques. The challenging issue in the synthesis of nanoparticles is over range of chemical compositions, size, and high monodispersity.

Zinc oxide nanoparticles have been synthesized in variety methods, such as green synthesis, sol-gel, thermal decomposition and precipitation methods makes it possible to obtain products with particles differing in shape, size and spatial structure. In the last decades, several sophisticated approaches have so far been used to synthesize Zinc Oxide nanoparticles (ZnO-NPs) which in turn utilized in many fields for different glitter applications widely. In doing so, there are different methods used to synthesize Zinc Oxide nanoparticles (ZnO-NPs) sol-gel method (Ghrib et al., 2021), chemical precipitation, hydrothermal reaction (Gadalla et al., 2018), the hydrothermal method (Pradeev et al., 2018).

2.4.1. Co-precipitation method

Co-precipitation takes place when any solution is supersaturated to form precipitates with another substance. In this method, an inorganic metal salt is dissolved in the solvent and these formed species are hydrolysed by adding a basic solution example NaOH or KOH. By the action of the cationic solution, solutions are condensed with each other to form a metal hydroxide precipitate. The formed precipitate has undergone several processes, such as filtration, annealing, and drying, to collect nanopowders of crystalline metal oxides. The main advantage of using this method is that it is very economical and metal oxide nanopowders can easily be synthesized. The co-precipitation process can be affected by several parameters such as pH, temperature, the concentration of the solutes, annealing, and effect of catalyst, reaction time, and drying for obtaining metal oxides nanostructures of different morphologies. Additionally, these synthetic routes have been popularly adopted to synthesize by using ZnO NPs due to their low cost and high yield of nanoparticles with uniform size (Devi & Velu, 2016a).

2.4.2. Sol-gel process

The sol-gel method is defined as a wet chemical route for the synthesis of colloidal dispersions (sols) of inorganic and organic-inorganic hybrid materials, particularly oxides and oxides-based hybrid at relatively low temperatures. This process involves a formation of an inorganic network of colloidal suspension sol followed by gelation of the sol solution to form a continuous liquid phase gel. Thus formed gel can be used to fabricate various nanomaterials and nanostructures such as powders, aerogels, xerogels, etc. Several precursors can serve as sol forming constitutes such as metal alkoxides, metal-organic compounds, salts of inorganic acids, salts of organic acids, etc. However, the most commonly used precursors are metal alkoxides; compounds in which a metal is bonded to one or more alkyl groups through an intermediate oxygen atom. The addition of an acid or base catalyst is also common in sol-gel processes to increase the rate of the reaction.

This method can be used for fabrication purposes, mainly of metal oxides, such as silicon. In this process, the monomers are converted into colloidal solutions acting as precursors for the gel formation using discrete particles. The precursors that can serve the function of precursor materials will undergo hydrolysis of and poly condensation processes to form M-O-M bonds. In the hydrolysis process, as the name suggests, the precursor will hydrolyze and attains a hydroxyl group typically through the reaction with water. Poly-condensation is the process in which hydrolyzed species combine to make inorganic polymer-like chains through the elimination of a water molecule. The sol-gel synthesis process of nanoparticles was released to form inorganic compound through chemical reaction of a certain solution. The benefits of using sol-gel method are that it generates a good rate of thermal stability, high mechanical stability, good solution resistance, and possibility to stimulate transformation (Parihar et al., 2018).

2.4.3. Thermal Decomposition

Thermal decomposition, or thermolysis, is a chemical decomposition caused by heat. The decomposition temperature of a substance is the temperature at which the substance chemically decomposes. Many oxides nanoparticles have been prepared by thermal decomposition, Likewise, zinc oxide nanoparticles prepared by thermal decomposition.

2.4.4. Biosynthesis

Biosynthesis of nanoparticles is a method of synthesizing nanoparticles using microorganisms and plants having biomedical applications. This approach is an environment-friendly, cost effective, biocompatible, safe, green approach (Abdul Salam et al., 2014). Green synthesis includes synthesis through plants, bacteria, fungi, algae etc. They large scale production of ZnO NPs free of additional impurities (Yuvakkumar et al., 2014). NPs synthesized from biomimetic approach show more catalytic activity and limit the use of expensive and toxic chemicals.

2.5. Characterization techniques of Zinc Oxide nanoparticles (ZnO-NPs)

To apply zinc oxide nanoparticles (ZnO-NPs) for any of the applications characterizations should be held after the synthesis of the material. Several physical techniques have been developed to characterize the size, morphology, and other remarkable properties of zinc oxide nanoparticles (ZnO-NPs). The most commonly used characterization techniques are X-ray diffraction (XRD), UV-visible (UV-Vis) Spectroscopy, Fourier Transform Infra-Red (FTIR) Spectroscopy, and Photoluminescence (PL) Spectroscopy.

2.5.1. X-ray Diffractometer (XRD)

X-ray diffraction (XRD) is a powerful non -destructive technique for characterizing crystalline materials. It provides information on structures, phases, preferred crystal orientations (texture), and other structural parameters, such as average grain size, crystallinity, strain, and crystal defects. X-ray diffraction peaks are produced by constructive interference of a monochromatic beam of X-rays scattered at specific angles from each set of lattice planes in a sample. The peak intensities are determined by the distribution of atoms within the lattice. Consequently, the X-ray diffraction pattern is the fingerprint of periodic atomic arrangements in a given material (Bunaciu & Aboul-enein, 2015). The X-ray diffraction (XRD) technique has been used in this study to characterize the crystalline structure of the powder samples; the XRD also provided information on unit cell dimensions. It is an efficient non-destructive analytical technique used for the identification of the crystalline structure of compounds by their diffraction pattern. A diffraction pattern is produced when a material is irradiated with a collimated beam of x-rays. In the X-ray source, fast-moving electrons are bombarded at the target metal (usually Cu or Mo) to generate X-ray as well as heat upon the rapid deceleration of electrons. The x-ray spectra generated by this technique provide a structural fingerprint of the material (unknown). The relative peak height is generally proportional to the number of grains in a preferred orientation and peak positions are reproducible.

XRD works on the principle that waves interacting with atomic planes in a material to form a diffraction pattern that is characteristic of the material’s structure. Furthermore, XRD analysis can easily detect the existence of defects in a particular crystal, its resistance level to stress, its texture, its size and degree of crystallinity, and virtually any other variable relating to the sample's basic structure (Bunaciu & Aboul-enein, 2015).

2.5.2. Ultraviolet-visible spectroscopy (UV-Visible)

UV-visible Spectroscopy is the type of absorption spectrophotometer which involves the excitation of electrons present in the molecule from the ground state to the excited state. It is the most reliable and accurate analytical method used to measure the scanning or transition of electron and optical properties of materials. An absorption spectrophotometer is an analytical technique in which compounds absorb light of radiation of a specific wavelength. UV-Vis spectroscopy is almost entirely used for quantitative analysis in which the estimation of the amount of a compound known to be present in the sample solution. The absorption spectra of atoms, molecules, or ions are generated when a beam of electromagnetic energy or light is passed through a sample and absorbs a portion of the photons of electromagnetic energy passing through the sample.

The absorption peak depends on some factors like selection of wavelength, nature of the solvent, bandgap, oxygen deficiency, size and structure of the nanoparticles, surface roughness, impurity centers, PH of the solution, and temperature. The bandgap energy, the energy required for the transition of an electron from a state of lower energy (E_1) to the state of higher energy (E_2) is equivalent to the energy of electromagnetic radiation (photon energy) that causes transition. The bandgap energy can be determined by substituting the value of the absorption peak at a given wavelength in the following Eq (2.13) (Salahuddin et al., 2015):

$$E_g = E_2 - E_1 = h\nu = h\frac{c}{\lambda} = \frac{1.240}{\lambda_{\max}}\left[keV\right] \tag{2.13}$$

where Eg is the bandgap energy (eV), h is Planck's constant (4.135667×10^{-15} eVs), c is the velocity of light (3×10^{8} m/s), and λ is the wavelength (nm) of absorption onset.
The optical bandgap Eg is determined from a Tauc-plot from the following Eq (2.14) (Pradeev Raj et al., 2017)

$$\alpha h\nu = A\left(h\nu - E_g\right)^n \tag{2.14}$$

where α is absorption coefficient, h is the Plank's constant, ν is the frequency of light radiation and Eg is the bandgap energy where 'n' takes the value of $1/2$ allowed direct transition.

2.5.3. Fourier Transformed Infra-Red (FTIR) Spectroscopy

Fourier transformed infrared spectroscopy (FTIR) is a technique used to get the information about the chemical bonding in a material. It is used to identify the elemental constituents of a material and it helps to get Structural identification and quantitative information about the synthesized nanoparticle (Muthukumaran & Gopalakrishnan, 2012).

2.5.4. Photoluminescence (PL) Spectroscopy

Photoluminescence (PL) corresponds to the luminescence resulting from the transitions of energy states in the material excited by electromagnetic radiation. When a material is irradiated by light with significant energy, photons are absorbed and electrons are excited to higher energy levels (excited states). Eventually, the electrons return to the lower energy states (equilibrium states), and the excess energy is released as photoluminescence or non-radioactively (e.g. phonons).

2.5.5. Scanning Electron Microscopy

Scanning electron microscopy (SEM) is a microscopic instrument which gives a detail information about size, external morphology (texture), microstructure of ZnO NPs. Electrons are thermionically emitted from a tungsten of lanthanum hexa boride cathode and are accelerated towards an anode; alternatively, electrons can be emitted via field emission. The electron beam, which has an energy ranging from a few hundred eV to 100 KeV, is focused by one or two condenser lenses into a beam. Characteristic X-rays are emitted when the primary beam causes the ejection of inner shell electrons from the sample and are used to determine the elemental composition of the sample. As most biological specimens are made up of non-dense material the number of secondary electrons produced is too low to be of much use in creating an image and therefore, they are usually coated with a very fine layer of a metal which readily produces secondary electrons. The back scattered electrons emitted from the sample can be used. These signals are monitored by photomultiplier tubes and magnified. An image of the investigated microscopic region of the specimen is observed in cathode ray tube and is photographed.

2.6. Applications of Zinc Oxide nanoparticles (ZnO-NPs)

Zinc oxide nanoparticles (ZnO-NP) recently have received much attention due to various applications such as UV absorption, deodorization, and antibacterial treatment (Moballegh, 2007). The synthesis of Zinc oxide nanoparticles (ZnO-NPs) through the different modes leads to the development of nanostructures with novel properties. These novel properties such as optical, structural, electrical, morphological, properties are prominently dependent on surface Plasmon and quantum confinement effect. Overall, Zinc oxide nanoparticles (ZnO-NPs) are of importance for fundamental research, and also relevant for various fields of industrial and high technological applications (Karakız et al., 2008).

2.6.1. Antibacterial applications of Zinc oxide nanoparticles (ZnO-NPs)

In this review, consolidate all the information regarding zinc oxide nanoparticles as an antibacterial agent has been attempted. The mechanism of interaction of zinc oxide nanoparticles against a variety of microbes has also been discussed in detail.

Metal oxides with antimicrobial activity include iron oxide (Fe_3O_4), titanium dioxide (TiO_2), copper oxide (CuO), and zinc oxide (ZnO). Amongst, ZnO has been studied widely in the literature for its antimicrobial activity. ZnO is also approved by the Food and Drug Administration (FDA) and listed as a generally recognized as safe (GRAS) material for its antimicrobial activity and low toxicity to the host and it is shown to be effective as a food additive.

It is universally known that zinc oxide nanoparticles (ZnO-NPs) are antibacterial and inhibit the growth of microorganisms by permeating into the cell membrane. Oxidative stress damages lipids, carbohydrates, proteins, and DNA (Siddiqi et al., 2018). Zinc oxide nanoparticles (ZnO-NPs) have been used as an antibacterial substance against Salmonella typhi and S. aureus in vitro. Of all the metal oxide nanoparticles studied thus far, zinc oxide nanoparticles exhibited the highest toxicity against microorganisms.

Surface modification and functionalization are other factors leading to potential changes in NPs antimicrobial activity. Some functionalization can increase the presence of oxygen atoms on NPs surfaces that can lead to more reactive oxygen species (ROS) production in the medium. Releasing ions from NPs as a result of NP modification is possible, which consequently increases NP antimicrobial activity through the ion toxicity mechanism. In addition, NP modification can lead to an increase of the surface area, and thus it increases the surface-area-to-volume ratio that results in increasing the NP antimicrobial potential. Coating NPs is one of the modification approaches, which may be lead to the presence of more toxic agents or enhances one of the antimicrobial mechanisms of NPs, and also induces surface defects (such as vacancy defects) in the NPs (Hoseinzadeh et al., 2017).

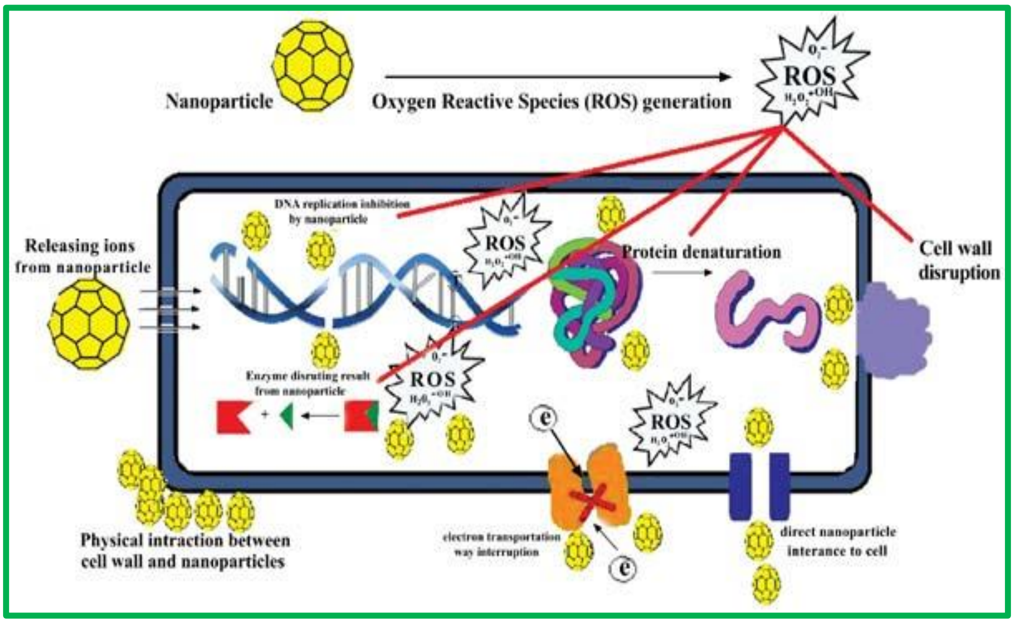

Figure 2.2: ROS and other mechanisms of antimicrobial activity of the metal NPs (Hoseinzadeh et al., 2017)

2.6.2. Application of Zinc Oxide Nanoparticle on Textiles

Zinc oxides nanoparticles used in textile finishing to alter surface properties and impart desirable textile functions. Nanosized particles have a larger surface area and their use can therefore result in higher efficiency of the treatment agent than larger size particles. Besides, nanosized particles are transparent, and do not affect the color and brightness of the textile substrates. fabrics treated with nanoparticles of ZnO, may replace fabrics treated with active carbon, previously used for chemical and biological protection (Sawhney et al., 2008).

The use of Zinc oxide nanoparticles in the textile industry has increased rapidly. This is mainly due to the fact that conventional methods used to impart different properties to fabrics often do not lead to permanent effects, and will lose their functions after laundering or wearing. Zinc oxide nanoparticles can provide high durability for treated fabrics, with respect to conventional materials, because they possess large surface area and high surface energy that ensure better affinity for fabrics and lead to an increase in durability of the textile functions. Wash fastness is a particular requirement for textile and it is strongly correlated with the nanoparticles adhesion to the fibers. In order to increase the wash fastness, the nanoparticles can be applied by dipping the fabrics in a solution containing a specific binder (Becheri et al., 2008); (Chang et al., 2010); (Gao et al., 2009); (Vigneshwaran et al., 2006).

Textile materials coated with these zinc oxide nanoparticles have proven to be useful for many applications, such as hydrophobicity, antimicrobial, ultraviolet (UV) protection and self-cleaning substrates. However, more interesting and progressive works in the field of textile finishes are the construction of bifunctional or multifunctional fabrics using various nanostructured materials. The finished fabrics can offer multiple innovative characteristics (antimicrobial, water repellent, self-cleaning, UV blocking, electrical conductivity, etc.) simultaneously, which broadens the practical areas of the final product (Hossain & Rahman, 2015)

2.6.3. Zinc Oxide Nanoparticles for UV-Protection Textiles

High exposure to UV radiation can result in skin damage such as sunburn, premature skin ageing, allergies, and even skin cancer, particularly in white-skinned people. However, zinc oxide nanoparticles coated textiles can provide effective protection against such damage. Sun protection textiles are common choices to protect against UV radiation although UV radiation also weathers and degrades textiles. So many UV blocking agents are being developed to add or to enhance the UV protection function of the textiles (Riva et al., 2006). There are both organic and inorganic UV blockers. The organic blockers are also known as UV absorbers as they absorb the UV radiation, whereas the inorganic blockers such as TiO_2 and ZnO efficiently scatter both UV-A and UV-B, the main cause of skin cancer. Compared with organic UV absorbers, inorganic blockers are now preferred due to their properties such as nontoxicity and chemical stability under UV radiation (A. Mishra & Malik, 2014).

The transmission data were used to calculate the UPF (ultraviolet protection factor) and the percent UV transmission, according to the following equations. The UPF is the ratio of the average effective irradiance calculated for skin to the average UV irradiance calculated for skin protected by the test fabric. It was calculated using mean percentage transmission in the UV-A region (315–400 nm) and mean percentage transmission in the UV-B region (280–315nm) with the following equation (Gambichler et al., 2002).

$$UPF = \int_{\lambda_1}^{\lambda_2} \frac{E(\lambda)S(\lambda)d\lambda}{E(\lambda)S(\lambda)T(\lambda)d\lambda} \tag{2.15}$$

$$\text{Percent UV transmission} = \frac{\sum_{\lambda_1}^{\lambda_2} T(\lambda)}{(\lambda_2 - \lambda)_1} \qquad (2.16)$$

Where $E(\lambda)$ is the relative erythermal spectral effectiveness, S (λ) is the solar spectral irradiance in $\mathrm{Wm^{-2}nm^{-1}}$ and T(λ) is the spectral transmission specimen obtained from UV spectrometric experiments. E(λ) and S(λ) obtained from the national oceanic and atmospheric administration data base (NOAA).

3. Materials and Methods

3.1. Materials, Chemicals, and Solvents

The chemicals used for synthesis of ZnO NPs were zinc nitrate hexahydrate (HiMedia, India), Polyvinyl Alcohol (HiMedia, India), sodium hydroxide (Alpha Chemika, India), zinc acetate dihydrate (UniChem, India), and leaf of a plant species (*Moringa oleifera)* collected from Adama, Ethiopia. The plant contains several phytochemical compounds in its natural extract. Also Culture media such as Mueller Hilton Agar (MHA) (M173-500G HiMedia India), Tryptone Soya Agar (TSA) (T131-500G HiMedia, India), and Nutrient Broth (N173-500 G HiMedia India) are used for cultivation of the test organisms. DMSO (99% Unichem, India) and double distilled water were used as the solvent. All chemicals are analytical grade standards. In addition, $ZnCl_2$ (Neolab, India), 1, 2- ethanediol, 2-propanol, NaCl, zinc nitrate (Zn $(NO_{3)2}.6H_2O)$ (Himedia, India), ammonium chloride (NH_4Cl), urea, ammonia solution, and ethanol were used in synthesis of zinc oxide nanoparticles of different shape, size and morphology. Cotton fabrics were purchased from Alameda Textile Factory (Addis Ababa, Ethiopia) and Local market (Adama, Ethiopia). The fabrics were washed and rinsed and dried before coating and *in situ* synthesis.

3.2. Methods to study the effect of temperature and polyvinyl Alcohol (PVA) concentrations on the structural and optical properties of zinc oxide nanoparticles

In order to prepare ZnO NPs by sol-gel method, 6 gm of Polyvinyl Alcohol was dissolved in 60 ml of double distilled water and stirred for 30 min until homogenous milk white solution obtained. Again 2 gm of zinc nitrate hexa-hydrate ($Zn(NO_3)_2.6H_2O$) also dissolved in 20 ml of double distilled water and stirred by magnetic stirrer for 15 min. Zinc nitrate hexa-hydrate ($Zn(NO_3)_2.6H_2O$) solution was added into chelating agent, Polyvinyl Alcohol (PVA) solution drop by drop at 70 ^{0}C under suitable magnetic stirring for 2 hrs. The mixture solution should be stirred till the gel like substances are formed. The gel sample was allowed to dry in an oven at 160 ℃ for 12 hrs. The sample was calcinated in muffle furnace (Model No: MC2-5/5/10-12, Biobase, China) at the temperature of 400-600 ^{0}C in open air for 8 hrs. The same procedure was followed to prepare PVA concentrations dependent (1.89, 2.27, and 3.34 M) ZnO NPs at the temperature of 400 ℃.

The X-ray diffraction (XRD) pattern for ZnO nanoparticles were analyzed using XPERT-PRO X-ray diffractometer by generating Cu-K_α radiation (λ=1.5418Å). It is used to determine the crystalline phase of the synthesized nanoparticles. An X-ray generator operates at a voltage of 40 kV and applied current of 30 mA at room temperature. Intensities were measured at room temperature for angle range of $2\theta = 10^0 \leq 2\theta \leq 80$. All the diffraction peaks are well indexed to the hexagonal ZnO wurtzite structure (JCPDS card no. 36-1451). The average nano crystalline size was calculated from the Debye Scherrer formula as follows Eq. (2.8).

The lattice parameters 'a' and 'c' and the spacing distance d_{hkl} for the wurtzite structure of ZnO can be calculated using the Eq. (2.4), (2.2), and (2.5).

The unit cell volume (V) of the hexagonal system was calculated by using the following formula Eq. (2.11)

The Zn-O bond length (L) and positional parameter in the wurtzite structure is given by Eq. (2.6) and Eq. (2.7)

The morphology of the resulting nanoparticles was characterized using Scanning Electron Microscope (Hitachi, H-7600, Japan). The optical absorption of the samples was measured by UV-Vis-NIR spectrophotometer (Perkin Elmer, Lambda, Ueberlingen, Germany) in the wavelength regions of 200-500 nm at 2 nm resolutions. The band gap energy of ZnO NPs is calculated using Eq. (2.13).

The vibrational spectra of ZnO NPs were measured by FT-IR (Perkin Elmer 65) in the range of wave number from 400-4000 cm^{-1}. The photoluminescence properties of ZnO NPs were measured by spectrofluorometer (Fluoromax-4, Spectrofluorometer) at room temperature with Xenon lamp as the excitation light source at resolution of 1 nm. The excitation and emission spectra are 264 and 380-500 nm respectively.

3.3. Methods of synthesis ZnO NPs using Chemical, Thermal and Green Route and their Application for Antimicrobial Activity

Different synthesis methods have been applied to get different morphology and optical properties of ZnO NPs. The sol-gel method of synthesized ZnO NPs prepared as follows.

6 gm of Polyvinyl Alcohol (PVA), ([-CH_2CHOH-]$_n$), were dissolved in 60 ml of double distilled water and stirred by magnetic stirrer for 30 min. Again 2 gm of zinc nitrate hexa-hydrate ($Zn(NO_3)_2.6H_2O$) were separately dissolved in 20 ml of double distilled water and stirred for 15 min. The solution of Zinc nitrate hexa-hydrate solution added into PVA solution drop by drop at 70℃ under suitable magnetic stirring for 2 hrs. The mixture solution stirred until the gel like substances formed; this gel type sample was allowed to dry in an oven at 160℃ for 12 hrs. The sample was calcinated in furnace for 8 hrs at the temperature of 400℃. By similar procedure, the other samples were prepared at calcinations temperature of 500℃ .

The thermal decomposition method of synthesis of ZnO NPs was performed according to the following procedure. 15 gm of the zinc acetate dihydrate was calcinated in muffle furnace at the temperature of 400^0C for 3 hrs reaction times without any special atmospheric condition.

The precipitation method of synthesis was carried out according to the following procedures. 12 gm of zinc acetate dihydrate, ($Zn (CH3COO)_2 .2H_2O$), was dissolved in 100 ml of double distilled water in a beaker and stirred for 30 minutes at the temperature of 60℃. Similarly, 3 gm of NaOH was dissolved in 40 ml of double distilled water in a separate beaker and stirred for 15 minutes. The solution of sodium hydroxide was added to zinc acetate dihydrate solution with constant stirring to form aqueous of milky white colloid solution. The reaction was allowed to proceed for 2 hrs after addition of sodium hydroxide. The solution was allowed to settle and dry in oven at 160℃ for 4 hrs. The sample calcined at 200℃ for 2 hrs reaction times in furnace without any special atmospheric condition. By similar procedure, other samples were prepared at the temperatures of 300 and 500℃, respectively.

The Green method of synthesis of ZnO NPs from *Moringa oleifera* leaves was prepared according to the following procedures. 12 gm of *Moringa oleifera* leaves were dissolved in 200 mL of double distilled water. The solution stirred for 20 min using magnetic stirrer at 60℃. The extracted Moringa oleifera leaf was used for synthesis of ZnO nanoparticles. 20 mL of leaf extracted solution added to 2 g of zinc nitrate hexa-hydrate ($Zn (NO_3)_2. 6H_2O$). The mixed solution stirred for 30 min at 80℃ and cooled at room temperature. The color of the solution turns to yellow and calcinated at 400℃ for 2 hrs in furnace. Finally, white powder was obtained.

In vitro antimicrobial activity of ZnO NPs was tested using agar well diffusion method against two gram-positive bacteria species (*S. aureus, B. subtilis,* and three gram-negative bacteria species (*E. coli, P. aeruginosa,* and *S. Typhi)* and one fungal species (yeast) (*C. albicans*). The strains were transferred to nutrient broth and incubated to grow aerobically at 37^0C for 24 hours until it achieved the turbidity of 0.5 McFarland standards. 0.01 ml of each sub-cultured bacteria and yeast test organisms were spread plated using sterilized cotton swab on 20 ml of sterilized molten and cooled MHA media and TSA media, respectively. Subsequently, agar wells of 5mm diameter were prepared on different plates with sterilized stainless steel cork borer and labeled properly. About $100\,\mu l$ of different concentrations (0.1 -106.24 mM) of ZnO were added into well using micropipette. The plates containing the microbes and ZnO nanoparticles were incubated at 37^0C for 24 h in case of bacteria and at 28^0C for 48 h in case of yeas. The plates were examined for evidences of zones of inhibition, which appear as a clear area around the wells. The diameter of such zones was measured using ruler and mean value for each organism recorded and expressed in millimeter.

The microbial activity of ZnO NPs was checked by determining the minimum inhibitory concentration (MIC) using agar dilution method. The MIC is the lowest concentration of nanoparticles that did not permit any visible growth of microbes during 24 h of incubation. After inoculation of target bacteria and fungi on MAH and TSA, respectively with different concentrations of NPs, the growth of test organisms were determined by counting colony forming unit (CFU) in each plate. The lowest concentration from which the bacteria and fungi do not grow when transferred to fresh medium is minimum inhibitory concentration (MIC). The standard antibiotic drug gentamicin and the sterile distilled water were used as positive and negative control respectively. All experiments were performed three times and the results were averaged.

3.4. Methods to Study the binding of Caffeic Acid (CFA) with ZnO Nanoparticles (NPs) using Spectroscopic Techniques

Stock solutions of caffeic acid ($1.05x10^{-3}$ mol L^{-1}) were prepared in sodium phosphate buffer solution (PH=6.8) and ZnO NPs dissolved in deionized water for steady state fluorescence and UV-Vis absorption measurements. The fluorescence measurements were carried out by successive addition of ZnO NPs (7.55-15.90) $x10^{-6}$ M to a fixed amount of caffeic acid ($1.72x10^{-5}$ M). Thus, spectra of series of solutions containing different amounts of ZnO NPs and definite amounts of caffeic acid were obtained. The mixed solutions were subjected to ultrasonic vibration for half hour. For the experiment carried out at the temperature of 295, 303 and 308 K solutions were kept in water bath to maintain the designed temperature of the solution.

The emission corresponding to λ_{exc} 300 nm for caffeic acid was recorded in the λ_{em} range of 350-580 nm. The excitation and emission slit width was set at 10 nm and scan speed 240 nm/min. From emission spectral analysis the quenching rate constant (k_q), the Stern-Volmer constant (k_{sv}) and thermodynamic properties of the interactions were determined. Furthermore, using Förster non-radative energy transfer theory the efficiency of energy transferred and distance between donor and acceptor were calculated. Similarly the UV-Vis absorption spectra were measured in the wavelength of 200-500 nm, by successive addition of ZnO NPs (7.55-15.90) $x10^{-6}$ M to a fixed amount of caffeic acid ($5.22x10^{-5}$ M) solutions in each tube. The FT-IR spectra of CFA in the presence and absence of ZnO NPs were recorded at room temperature (298 K) in the range of 600-4000 cm^{-1}. The mean hydrodynamic particle size distribution of CFA ($C=1.72x10^{-5}$ M) were measured in the absence and presence of ZnO NPs ($C=7.55x10^{-6}$, and $1.3x10^{-5}$ M) setting the temperature of the solvent at 25 ^{0}C. In order to get more insight on the interaction of the biomolecules and NPs the TEM measurement monitored for ZnO NPs ($C=1.76x10^{-1}$ M) and its mixture with CFA ($C=1.055x10^{-3}$).

3.5. Methods of Incorporation of Zinc oxide nanoparticles in cotton textiles for UV light protection and antimicrobial activities

ZnO nanoparticle (S-1) was synthesized by precipitation method according to the procedures reported elsewhere (Moroni et al., 2005). 5.5 g of $ZnCl_2$ was dissolved in 200 ml deionized water in beaker and vigorously stirred by magnetic stirrer at 90^{o}C then 16 ml of 5 M NaOH aqueous solution were added drop wise to the zinc chloride solution, with a gentle stirring over a period of 10 min at 90^{o}C. After the reaction is complete, the solution was allowed to settle and the supernatant solution was removed and the remaining suspension was washed 5 times with distilled water. The particles were then peptized with 2-propanol at room temperature in order to disrupt microagglomerates (Pérez-Maqueda et al., 1998). The synthesized particles were then collected by centrifugation at 4000 *rpm* for 10 min. Finally the prepared particles were treated thermally in oven for 5 hrs at 250 ^{0}C which leads to the formation of Zinc oxide nanoparticles. Similarly, the second synthesis (S-2) also followed same procedures with above method but carried out in different solvent (1, 2-ethanediol) and temperature of 150 ^{0}C.

For the application of NPs on cotton fabrics, (10 cm × 10 cm) cotton sample was immersed in to the the dispersion of ZnO NPs (synthesized using (S-1 and S-2)) in 2-propanol (5 % w/w) under gentle magnetic stirring. The cotton fibers were then squeezed to remove the excess dispersion and dried in oven at 130 °C for 15 min under atmospheric pressure (dry heat). In order to evaluate the nanoparticles adhesion to the cotton fibers, the treated fabrics were washed two times.

The *in situ* method of synthesized zinc oxide nanoparticles (S-3) on cotton fabrics was performed according to the developed procedure mentioned elsewhere (Pérez-Maqueda et al., 1998) . First the fabric was washed in warm water using a non-ionic detergent to ensure removal of residual chemicals. The washed fabric was rinsed with warm water and dried in oven at 75 ^{o}C for 60 min. It was then, transferred in to 100 ml of 0.005 M of $Zn(NO_3)_2.6H_2O$. After 15 min, 0.02 mol NH_4Cl, 0.01 M urea and 5 ml ammonia solution were added to the reaction vessel. The system was rapidly heated (10 ^{o}C/ min) to 90 ^{o}C and kept for 60 min under magnetic stirring (300 *rpm*). After the reaction is completed, the fabric was rinsed several times using distilled water and finally it was kept in oven at 150 ^{o}C for 10 min to ensure particles' adhesion to the fibers' surface.

The UV light responses of the treated and untreated cotton fabrics were studied using a UV-Vis spectroscopy. The effectiveness in shielding UV radiation was evaluated by measuring the UV absorption, and Transmission. The transmission data were used to calculate the ultraviolet protection factor (UPF) and the percent of UV transmission, according to Eq. (3.7-3.8) (Gambichler et al., 2001)

The antibacterial activity of the zinc oxide nanoparticles synthesized by (S-1) and (S-2) are applied on *Gram positive (S. aureus)* and Gram negative (*E. coli)* bacteria with Identification code (ATCC 25922) and (ATCC25923) respectively using agar disc diffusion method (Sawai, 2003). Microbial strains were grown aerobically in nutrient broth for 24 hr at 37 °C until the turbidity of bacterial suspensions was achieved to 1.3 × 10^{8} CFU ml^{-1} (0.5 McFarland Standard). Sterile standard filter paper discs (6 mm in diameter) were impregnated with sterile aqueous suspensions of ZnO NPs at 126 µg/ml, 252µg/ml,504 µg/ml and 1280 µg/ml were prepared in dimethyl sulfoxide (DMSO) and placed onto the inoculated plates using sterile forceps. The standard antibiotic drug Ciprofloxacin was used as positive control. The plates were incubated at 37°C for 24 hrs. All measurements were performed in triplicate. Finally, the zone of inhibition formed around the discs was measured in millimeters (mm) and recorded.

Similarly, the antibacterial activity of the *in situ* synthesized ZnO NPs on cotton fabrics applied against both *Gram negative* (*Escherichia coli*) and *Gram positive* bacteria (*Staphylococcus aureus*) using agar diffusion method. The cotton fabrics with 20 mm of diameter were uniformly pressed on the agar and incubated for 24 h at 37 ^{0}C. After incubation, the antibacterial effect of the fabrics was investigated by evaluating zone of inhibition formed around the discs measured in millimeters (mm) and recorded.

4. Results and Discussion

4.1. Effect of temperature and polyvinyl Alcohol (PVA) concentrations on the structural and optical properties of zinc oxide nanoparticles

4.1.1. X-ray diffraction

The XRD patterns of ZnO NPs synthesized by the sol-gel method at different annealing temperature of 400, 500 and 600 °C shown in Fig.4.1. All XRD diffraction peaks of ZnO powders are in a good agreement with wurzite structure (hexagonal phase, space group $P6_{3mc}$) with lattice parameters a=b= 3.249 A^0 and c= 5.206 A^0 as reported in (JCPDS card no. 36-1451). Nine characteristic peaks were appeared at $2\theta =$ 31.802°, 34.468°, 36.306°, 47.600°, 56.592°, 62.951°, 66.411, 67.91 69.152° corresponding to (100), (002), (101), (102), (110), (103), (200), (112) and (201) of crystal planes. The samples (101) peak is the most intense peak that shows the plane is a preferred growth plane. The diffraction peak intensity also markedly increases with annealing temperature as shown in Fig. 4.1a-c. This may indicate that high annealing temperature provides sufficient energy to crystallites to orient in proper equilibrium sites and causes an increase in intensity (Raoufi, 2013). The average crystal sizes of ZnO NPs were calculated by Debye Scherrer formula using Eq. (2.8) based on the full width at half-maximum (FWHM) of the peaks and is shown in the Table 4.1. The average crystal sizes of ZnO NPs at annealed temperature of 400, 500 and 600 ℃ are 22 nm, 24 nm and 29 nm respectively. This result shows that, the average crystal sizes of ZnO NPs increased as the annealing temperature increased which is in good agreement with the result reported previously by (Preethi et al., 2016); (Singh et al., 2011); (Liu et al., 2016); (Hench & West, 1990). The thermal annealing lead to an improvement in the crystallinity and associated with increase in crystal size, diffraction intensity as well as increase in both the Zn-O bond length and unit cell volume as shown in Table 4.2. On other hand, the Full-Width at Half Maxima (FWHM) of ZnO NPs decreases as the annealing temperatures increased.

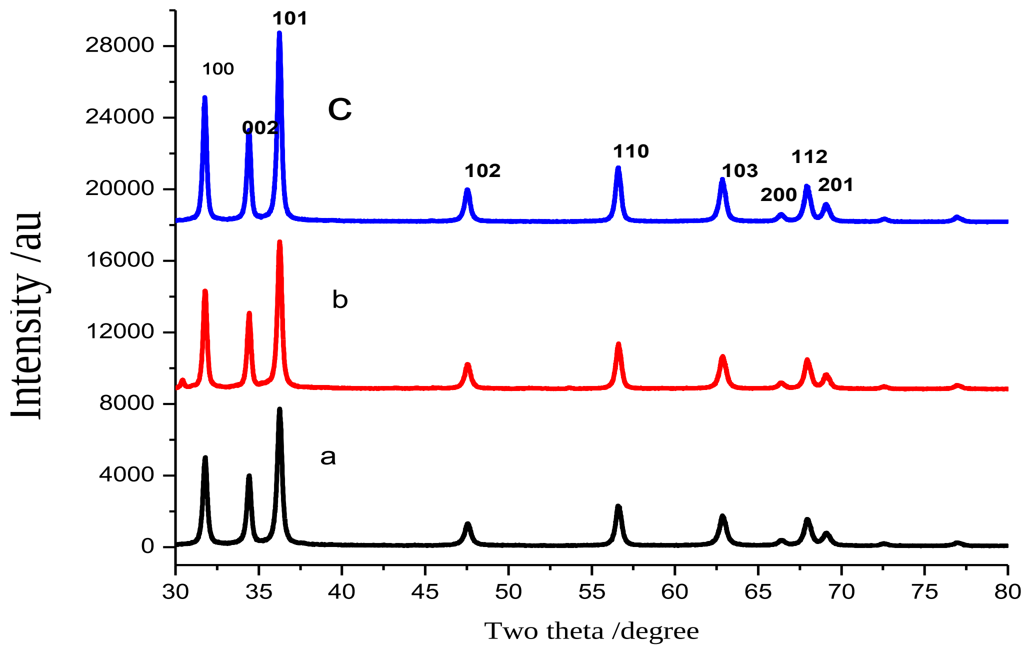

Figure 4.1: XRD patterns of ZnO NPs synthesized at annealing temperatures of (a) 400℃, (b) 500℃, and (c) 600℃, respectively.

The effects of annealing temperature on the lattice and others parameter of ZnO NPs were calculated using Eq. (2.2-2.7) and shown in Table 4.2. The lattice parameters are temperature dependent i.e. an increase in temperature leads to expansion of lattice parameters. The lattice parameters of pure zinc oxide reported by (JCPDS card no. 36-1451) are a= 0.325 nm and c= 0.521 nm are match with value obtained for ZnO NPs synthesized in this research. In addition, the nearly constant value of c/a ratio confirms that annealing of ZnO nanostructure does not make noticeable deformation in the lattice constant.

Table 1Table 2Table 4.1: Crystal size of ZnO NPS estimated using Debye –Scherer formula at the temperature of 400℃, 500℃, and 600℃,

Temperature/ ^{0}C	Particle size (D)/nm
400	**22 ±3**
500	**24 ±3**
600	**29 ±6**

Table 4.2: Lattice parameter, spacing distance, unit cell volume and bond length of synthesized ZnONPs at different annealing temperatures.

Temperatures	hkl	lattice parameter			d_{hkl} (nm)	V($A^{0\,3}$)	L(A^0)
		a(nm)	c(nm)	c/a			
400°C	101	0.2857	0.4952	1.733	0.1871	35.00	1.7871
500°C	101	0.2859	0.4955	1.733	0.1872	35.07	1.7887
600°C	101	0.2860	0.4957	1.733	0.1873	35.11	1.7892

Fig. 4.2 shows XRD patterns of ZnO NPs synthesized by changing concentration of PVA solution (1.89, 2.27 and 3.34M) at 400°C respectively. The X-ray diffraction peaks of ZnO NPs with different concentrations are 2θ = 31.99°, 34.45°, 36.32°, 47.60°, 56.86°, 62.93° and 67.86° which correspond to reflecting from (100), (002), (101), (110),(120),(103) and (112) of crystal planes respectively. The calculated average crystal sizes of ZnO NPs are 19, 22 and 24 nm for PVA concentrations of 1.89, 2.27 and 3.34 M respectively as shown in Table 4.3. The particle sizes, diffraction intensity and lattice parameters of ZnO NPs were increased as the PVA concentrations increased due to an increase in the number of molecules that required minimum energy.

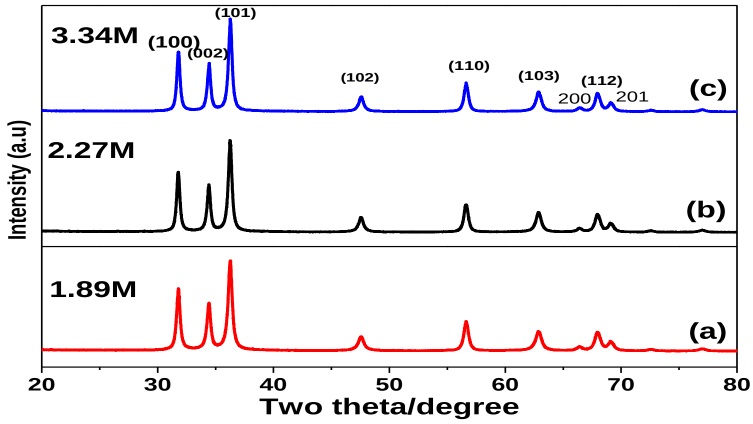

Figure 4.2: XRD patterns of ZnO NPs synthesized using various PVA concentrations,a) 1.89M, b) 2.27M and c) 3.34M.

Table 4.3: Average crystal size of ZnO NPS at different PVA concentrations.

Concentration (M)	Particle size (D)/nm
1.89	**19 ±6**
2.27	**22 ±4**
3.34	**24 ±3**

Table 4.4: Lattice parameter, spacing distance and unit cell volume of ZnO NPs at different PVA concentrations.

Concentrations	Hkl	Lattice constant			d_{hkl} (nm)	V(A^3)
		a(nm)	c (nm)	c/a		
1.89 M	101	0.2856	0.4950	1.733	0.2212	34.96
2.27 M	101	0.2858	0.4952	1.732	0.2213	35.03
3.34M	101	0.2859	0.4955	1.733	0.2215	35.07

4.1.2. Scanning Electron Microscopy (SEM) Analysis

Fig. 4.3 (a-b) shows the SEM images of the synthesized ZnO NPs using PVA as reducing agent at annealing temperatures of 400 ^{0}C and 500 ^{0}C respectively. As shown the figures morphology of the particles is uniform and has spherical shape. Also particles size and agglomeration of ZnO NPs increased as annealing temperature increased; this indicates the formation of larger particle sizes with small surface area to volume ration of NPs (Raoufi, 2013).

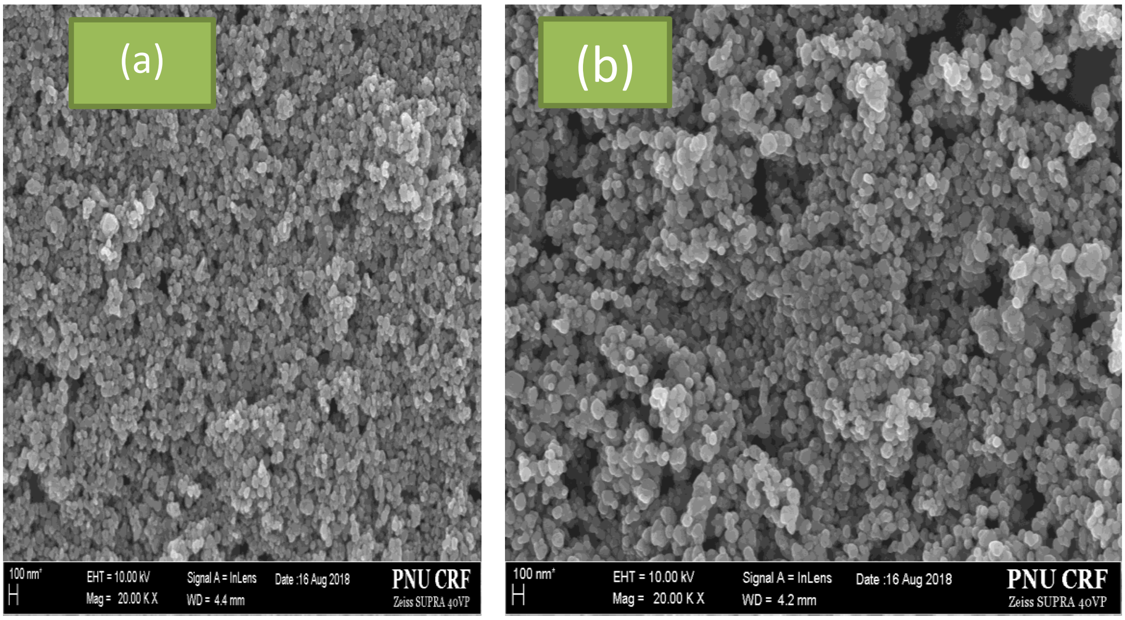

Figure 4.3: Scanning Electron Microscope images of ZnO NPs at (a) 400°C and (b) 500°C of annealing temperatures.

4.1.3. Fourier transform infrared (FT-IR) Spectroscopy

Fig. 4.4 shows the FTIR spectra of ZnO NPs measured in the wavenumber ranges of 400-4000 cm^{-1} at different annealing temperature. The broad and sharp band observed around 3447 and 1597 cm^{-1} are the characteristics of hydroxyl (OH) group (Jamdagni et al., 2018) ; (M. T. Ahmed et al., 2016). The small band found in the regions of 1718-1745 cm^{-1} are belong to C=O stretching vibration of carboxylic acid attached from PVA. The peaks observed in the regions of 2915-2940 cm^{-1} are belonging to C-H stretching. The intensity of the bands is significantly reduced at annealing temperature of 600 ^{0}C due to removal of functional groups and the formation of pure wurtzite structure.

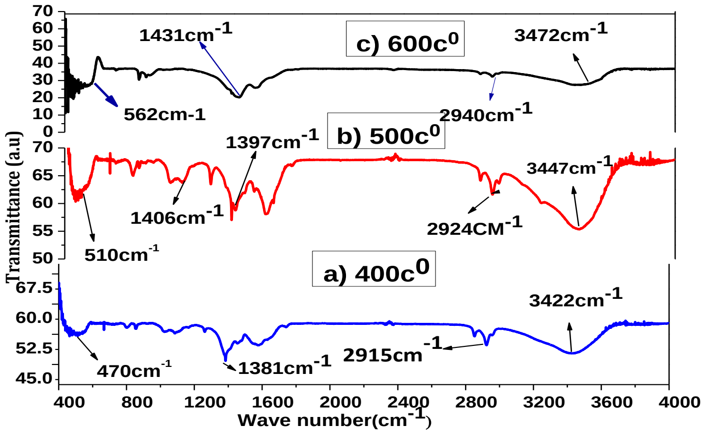

Figure 4.4: FT-IR spectra of synthesized ZnO NPs at different annealing temperatures.

Similarly, the FT-IR spectra of measured ZnO NPs by varying the concentrations are shown in Fig. 4.5 below. From the graph, the broad band observed in the region of 3200-3600cm^{-1} is due to the presence of hydrogen bond (O–H) vibration. Presence of O-H group represents the presence of water molecules on the surface of ZnO nanoparticles (Y. Wang et al., 2010); (S. K. Mishra et al., 2012). Similarly, the transmission peaks observed in the region of 2800- 3200cm^{-1} are due to C-H stretching frequency of alkyl groups. The strong peak position observed in the range of 445-556 cm^{-1} was attributed to characteristics of ZnO wurtzite structure (S. K. Mishra et al., 2012). In general shifting in peaks positions were observed as the temperature and concentration of PVA samples are changed.

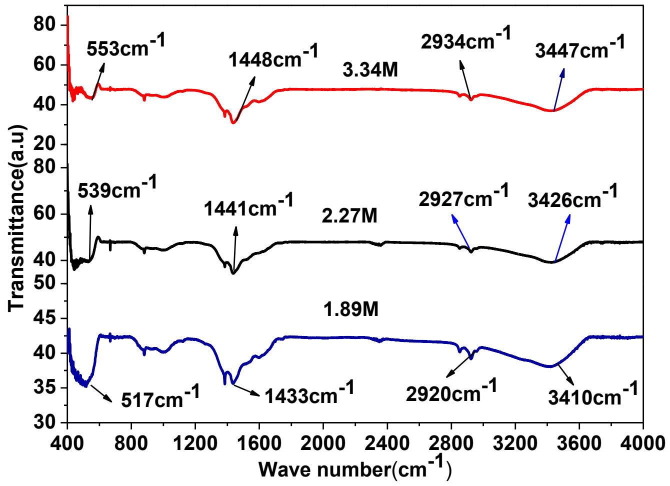

Figure 4.5: FT-IR spectra of synthesized ZnO NPs at 1.89, 2.27 and 3.34M PVA concentrations.

4.1.4. UV-Vis spectroscopy

Fig. 4.6 shows UV-Vis absorption spectra of ZnO NPs at different annealing temperatures. The absorption peak was observed at 370 nm, 377 nm and 382 nm for annealing temperatures of 400, 500 and 600 ℃ respectively. As temperature increased peak absorbance wavelength shifted to red due to decreasing in quantum confinement of the particles. The peaks are due to electronic transition from valence band to conduction band (Y. Wang et al., 2010). The band gap energy of ZnO NPs calculated using Eq. (2.13) were found to be 3.314, 3.251 and 3.176 eV for 400 500 and 600 ℃ respectively. The band gaps energy of ZnO NPs decreased with increasing temperature due to various particle sizes.

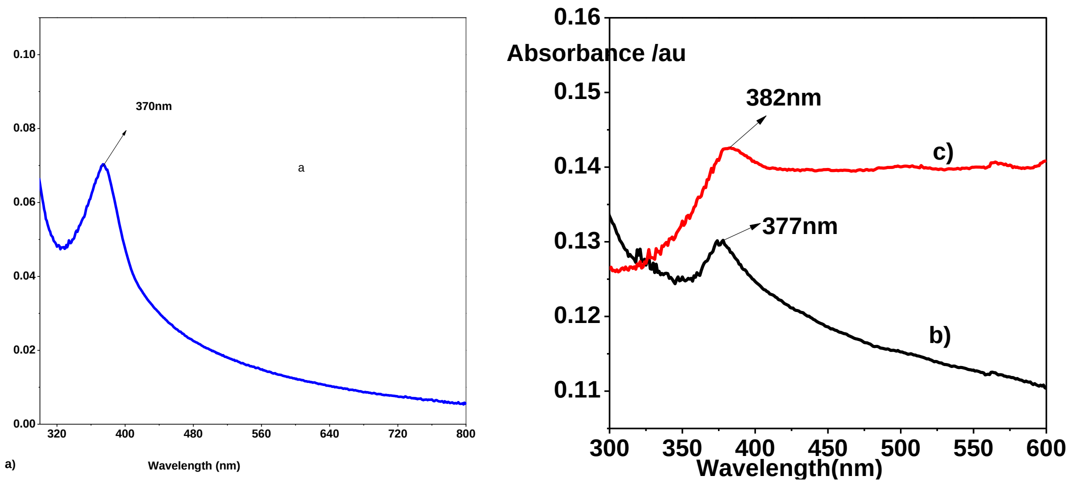

Figure 4.6: UV/vis Spectra of synthesized ZnO NPs at a) 400°C b) 500°C and c) 600°C.

Similarly, the absorption spectra of ZnO NPs synthesized using different PVA concentrations were shown in the Fig. 4.7. The peak absorption spectra of ZnO NPs were observed at 372, 377 and 380 nm for PVA concentrations (1.89, 2.27 and 3.34 M) respectively. The energy band gaps of ZnO NPs were decreased as the PVA concentrations increased. The red shift spectra of ZnO NPs as the PVA concentrations increase were in a good agreement with a literature reported by (Y. Wang et al., 2010).

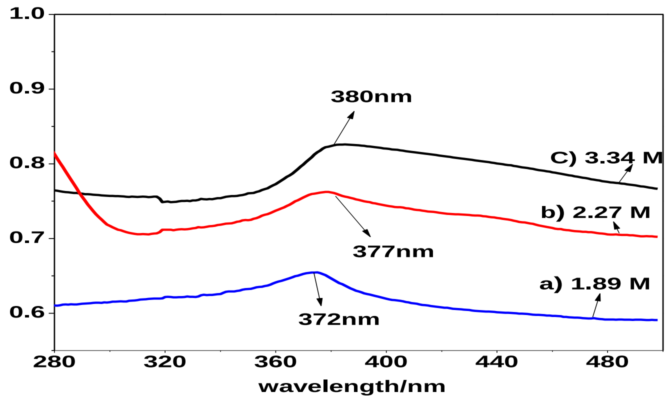

Figure 4.7: UV-Vis Spectra of synthesized ZnO NPs at different PVA concentrations a, 1.89 b, 2.27 and c. 3.34 M respectively

4.1.5. Emission spectral analysis

Fig. 4.8 (a-b) shows the emission spectra of ZnO NPs at annealing temperatures of 400 and 500°C. Generally the emission spectra of ZnO NPs consist of two emission bands: one in the UV-region near 370-400 nm and the other broad band in the visible regions 400- 700 nm. Our samples exhibited UV emission peaks at 396 nm, broad peaks at 413 and 418 nm (violet region) and other peaks at 449, 466,480 and 490 nm (blue region) respectively. The emission in the UV region is attributed to the recombination between the electrons in the conduction band and holes in the valance band. The violet emission at 417 nm is ascribed to an electron transition from a shallow donor level of neutral Zn_i to the top level of valance band (S. K. Mishra et al., 2012) The blue emission centered on 450 nm is attributed to singly ionized V_{Zn}^-. A blue green emission centred at 481 nm is due to radiative transition of electron from the shallow donor level of Zn_i to an acceptor level of neutral V_{zn}. The green emission which is not recorded in our sample is attributed to radiative transition from conduction band to the edge of the acceptor level of O_{Zn} caused by oxygen antisites (O_{Zn}) (S. K. Mishra et al., 2012). The peak emission of our samples is independent of the temperature but emission intensity is temperature dependent i.e. it increased as the temperatures of the samples increased.

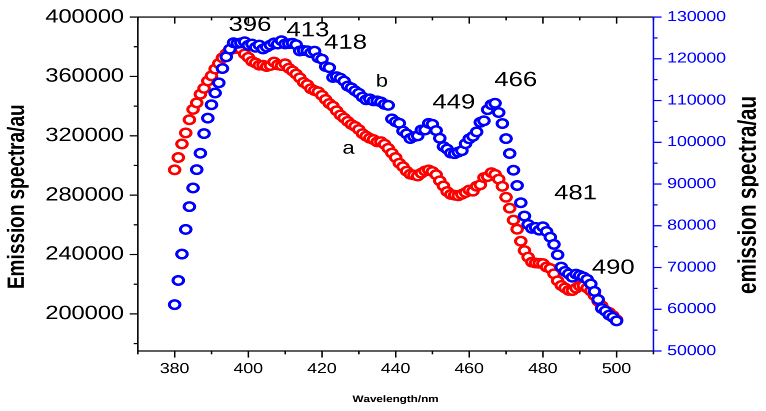

Figure 4.8: Emission spectra of synthesized ZnO NPs at a) 400°C b) 500°C.

4.2. Antimicrobial Activity of Chemical, Thermal and Green Route-derived Zinc Oxide Nanoparticles: A Comparative Analysis

4.2.1. X-ray diffraction analysis

The XRD pattern of ZnO NPs synthesized by sol-gel, thermal decomposition, precipitation and green methods are shown in Fig. 4.9 (a-e). All diffraction peaks are in a good agreement with wurzite structure (hexagonal phase, space group $P6_{3mc}$) with lattice parameters a=b= 3.249 A^0 and c= 5.206 A^0 as reported in (JCPDS card no. 36-1451). The nine characteristic peaks were appeared at $2\theta =$ 31.802°, 34.468°, 36.306°, 47.600°, 56.592°, 62.951°, 66.411, 67.91 69.152° corresponding to (100), (002), (101), (102), (110), (103), (200), (112) and (201) of crystal planes. The diffraction peak (101) is the most intense peak indicated that the preferred growth plane. The diffraction peak intensity also markedly increases with calcination temperature for NPs synthesized by same procedures. The calcinations temperatures lead to an improvement in the crystallinity and associated with increase in crystal size, and diffraction intensity. On other hand, the Full-Width at Half Maxima (FWHM) of ZnO NPs decreases as the temperatures increased (Belay et al., 2019); (Ghosh & Sharma, 2013). The result also indicated the increment in crystal size of ZnO NPs as the calcination temperature increased are in good agreement with the result reported previously by (Preethi et al., 2016); (Parra & Haque, 2014); (Alibe et al., 2017).

The average crystal size of ZnO NPs were calculated using Debye Scherrer formula, Eq. (2.8) based on the full width at half-maximum (FWHM) of the peaks shown in the Table 4.5. The average crystal size of ZnO NPs synthesized using sol-gel, thermal decomposition precipitation methods are in the ranges of 22-42 nm. On the other hand, crystalline size synthesized using green method is 8 nm. The study result indicated that the existence of size difference between green and chemical method.

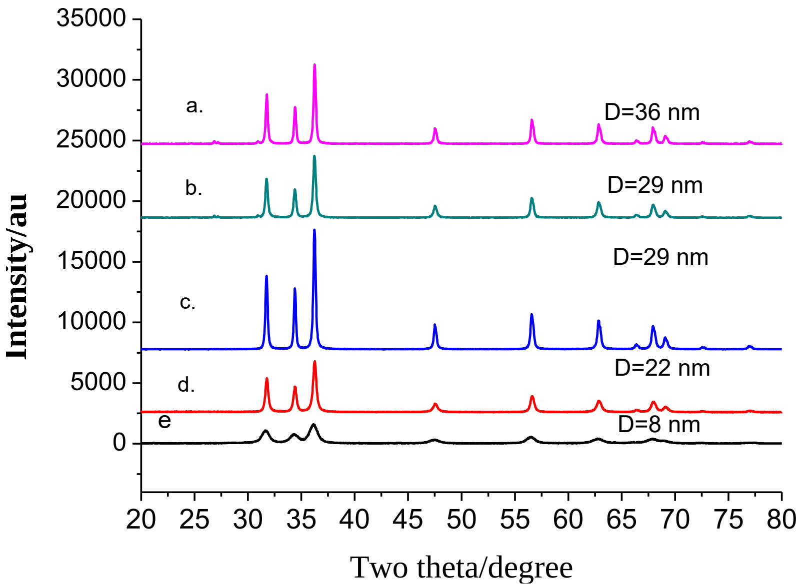

Figure 4.9: XRD patterns of ZnO NPs synthesized using (a, b) Precipitation at calcinations temperature 400°C and 500°C c) Thermal decomposition at 400°Cfor three hours d) sol-gel method at calcinations temperature of 400 0C e) Green synthesis method

The lattice parameters 'a', 'c' and the plane spacing distance (d_{hkl}) calculated using the Eq. (2.4-2.7) and tabulated in Table 4.5. The calculated results are consistent with standard of ZnO wurzite structure (hexagonal phase, space group $P6_{3mc}$) which has lattice parameters a=b= 3.249 A^0 and c= 5.206 A^0 as reported in (JCPDS card no. 36-1451). The unit cell volume of ZnO NPs estimated using Eq. (2.11) and shown in table 4.5. From table 4.5 it has been observed there is significant decrease in unit cell volume as the calcination temperature increased especially for NPs synthesized using precipitation method. This may be due to the fact that there are large numbers oxygen vacancies and vacancy clusters.

Table 4.5: Lattice parameter, interplanar spacing, crystal size and unit cell volume of ZnO NPs synthesized using sol-gel, thermal decomposition and precipitation method at different calcinations temperature

Synthesized ZnO NPs	Lattice parameters			$V (A^0)^3$	$d_{(101)}$(nm)	Crystal size (nm)
	a(nm)	c(nm)	c/a			
Sol-gel at 400 ^{0}C	0.3246	0.52072	1.6041897	47.513	0.247749074	22.04 ± 2
Sol-gel at 500 ^{0}C	0.3252	0.520963	1.6019772	47.711	0.24774905	29.38 ± 2
Thermal decomposition 400 ^{0}C	0.3252	0.520981	1.6020325	47.713	0.247746451	29.30 ± 4
Precipitation at 200 ^{0}C	0.32501	0.520812	1.6024491	47.642	0.247628754	29.92 ± 1
Precipitation at 300 ^{0}C	0.3249719	0.520561	1.6023577	47.578	0.247507575	36.90 ± 3
Precipitation at 400 ^{0}C	0.3252688	0.495621	1.5237274	45.410	0.244908146	41.67 ± 2
Green method (M1)	0.34433	0.52112	1.5314	53.506	0.258822	8.88 ±0.63

4.2.2. Scanning Electron Microscopy (SEM) and DLS analysis

The SEM images of ZnO NPs synthesized by sol-gel, thermal decomposition, precipitation and green methods are shown in Fig. 4.10(a-d). The morphology of ZnO NPs synthesized using precipitation and sol-gel methods are well dispersed spherical shape and their size are also in agreements with XRD results. On the other hand, uniform rod shape was observed for NPs synthesized using thermal decomposition method. Similarly, NPs synthesized using green method indicated the aggregation of thinner nanosheets to form nanosheet networks, where individual sheet have large lateral dimension. The present results of SEM are in a good agreement with (Awwad et al., 2014) the documented for green synthesized ZnO nanosheets and nanoflowers.

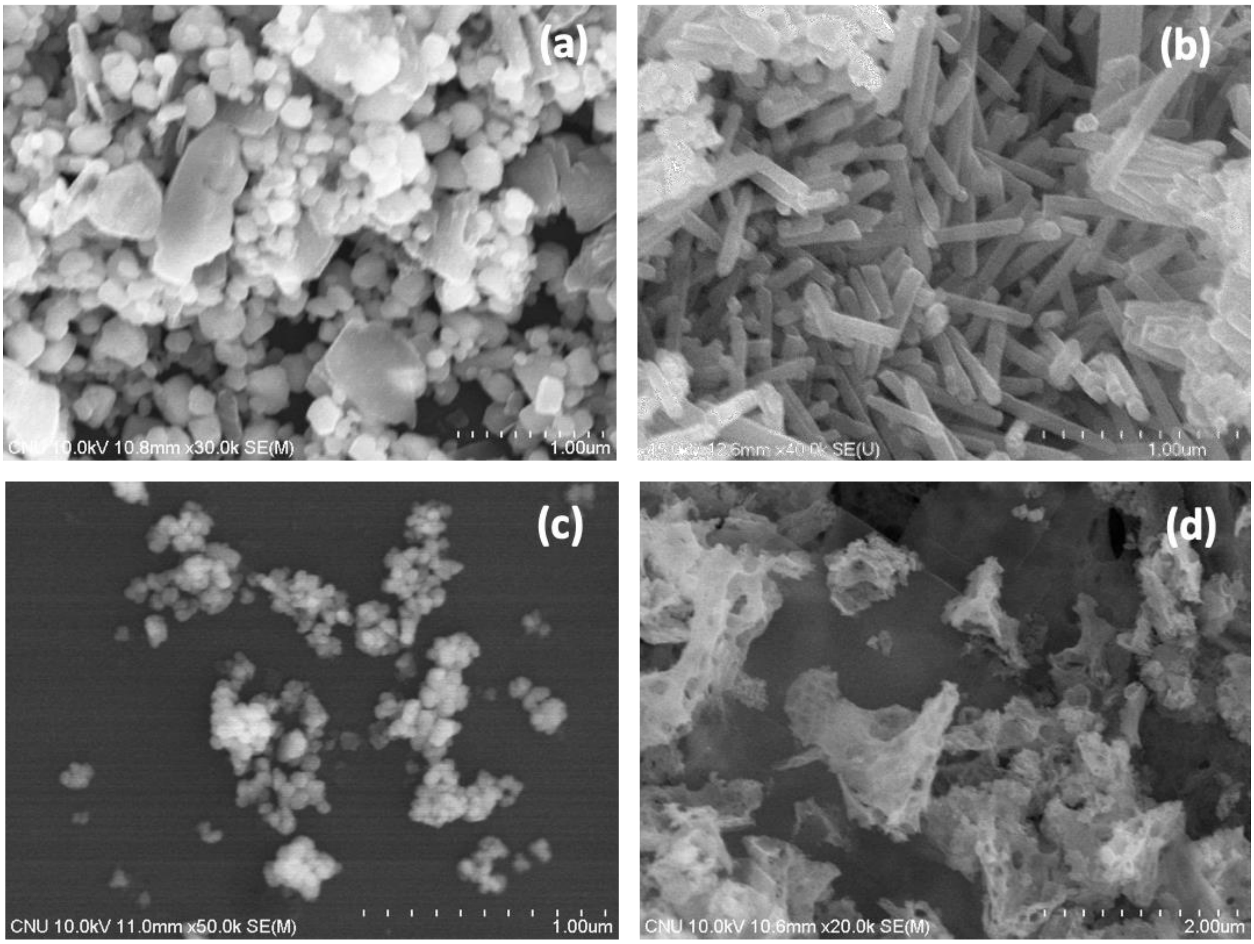

Figure 4.10: Scanning Electron Microscope image of ZnO NPs synthesized using a) Precipitation at calcinations temperature 400℃ b) Thermal decomposition at 400℃ for three hours c) sol-gel method at calcinations temperature of 400℃ d) green synthesis method

The size distribution profile of chemically synthesized of ZnO NPs, which has been done via DLS measurements, is shown in Fig 4.11(a-b). A maximum intensity at the average particle size of 223 and 345 nm for thermally decompose and precipitation methods were obtained. Particles size distribution of NPs can be influenced in several ways: sonification, adding stabilizers, and dispersant. The increase in the size of NPs in both methods is due to low viscosity of water result in high agglomeration as compare to other solvent like ethylene glycol.

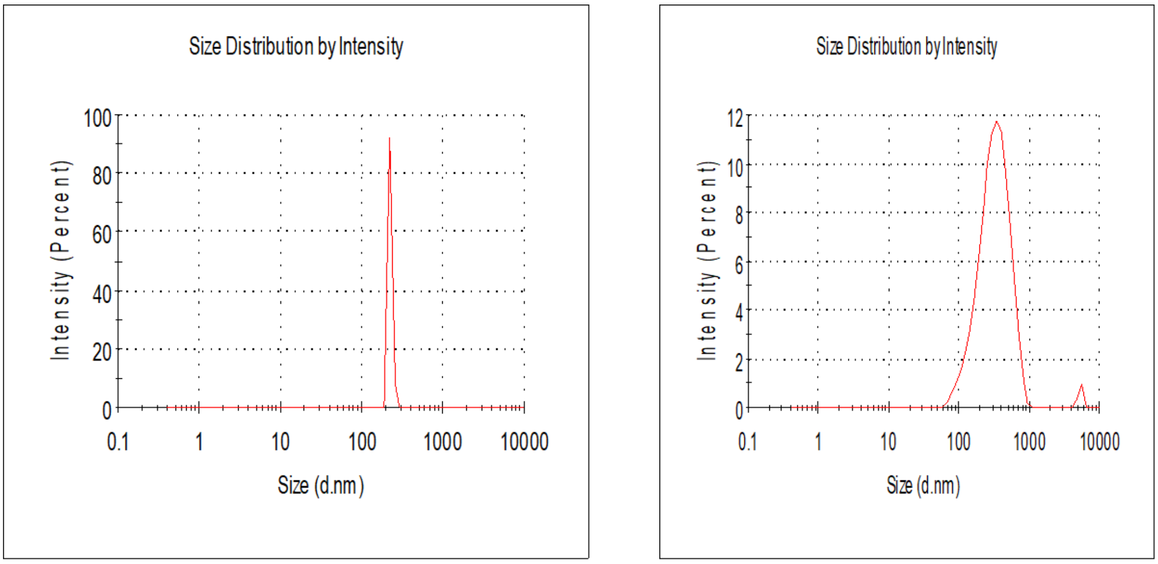

Figure 4.11: DLS size distribution of ZnO NPs synthesized using a) thermal decomposition method b) precipitation method

4.2.3. UV-Vis absorption analysis

The UV–visible absorption spectra of ZnO NPs synthesized by sol-gel, thermal decomposition, precipitation and Green methods are shown Fig. 4.12 (a-e). The absorption peaks of the samples were observed in the wavelength region of 344 - 377 nm. The corresponding optical band gap energy calculated using Eq. (2.13) is found to be in the range of 3.29-3.60 eV. ZnO NPs synthesized using green method has higher band width (3.6 eV) as compared to the chemically synthesized NPs. The absorptions peaks are related to the electronic transition from valance band to conduction band. All ZnO NPs samples exhibit blue shifted absorbance peak as compared to their bulk counterpart having absorbance peak at 386 nm (3.2 eV) at room temperature (M et al., 2009); (Talam et al., 2012). Also, blue shifts in the peak of absorbance were observed as the size of the particle decreased, due to increase in quantum confinement of the particle.

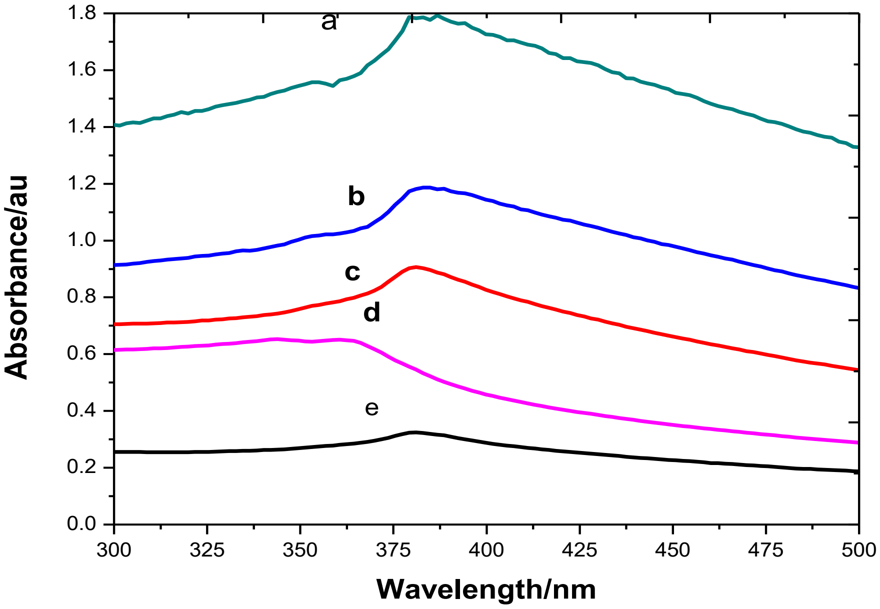

Figure 4.12: UV/Vis absorption spectra of ZnO NPs synthesized using (a, b) Precipitation method at 200^{0}C($\lambda_{\max} = 376\ nm$) and 300^{0}C ($\lambda_{\max} = 377\ nm$) calcinations temperature c) Thermal decomposition method at 400 ^{0}C for three hours ($\lambda_{\max} = 375\ nm$) d) Green method ($\lambda_{\max} = 344\ nm$) and e) Sol-gel method at 400^{0}C calcinations temperature ($\lambda_{\max} = 374\ \ nm$)

4.2.4. Emission spectra analysis

Figure 4.13 (a-e) shows the emission spectra of ZnO NPs synthesized by different methods. The emission spectra exhibit two bands: one is in the UV region (390-400 nm) and the other is in the visible region (420–650 nm). The samples were exhibited sharp UV emission peaks at 398, 400 and 390 nm which attributed to the recombination of electrons in the conduction band and holes in the valance band (Raji & Gopchandran, 2017) . The UV emission intensity of ZnO NPs synthesized using chemical methods are increase with the decrease of size of the particles as shown in Fig.4.13 (b-e). The results are evaluated in terms of intrinsic particle absorption and the number concentration of particles. It is shown that the particles become opaque for particle size greater than 70 nm. For larger size the absorbance decreases with increasing size due to the decrease in particle concentration. The visible emission spectra of the samples consisting different peaks in the violet and blue regions (420, 464, 666, 474, 484) are basically due to transition of electron from CB to VB and shallow level to deep level.

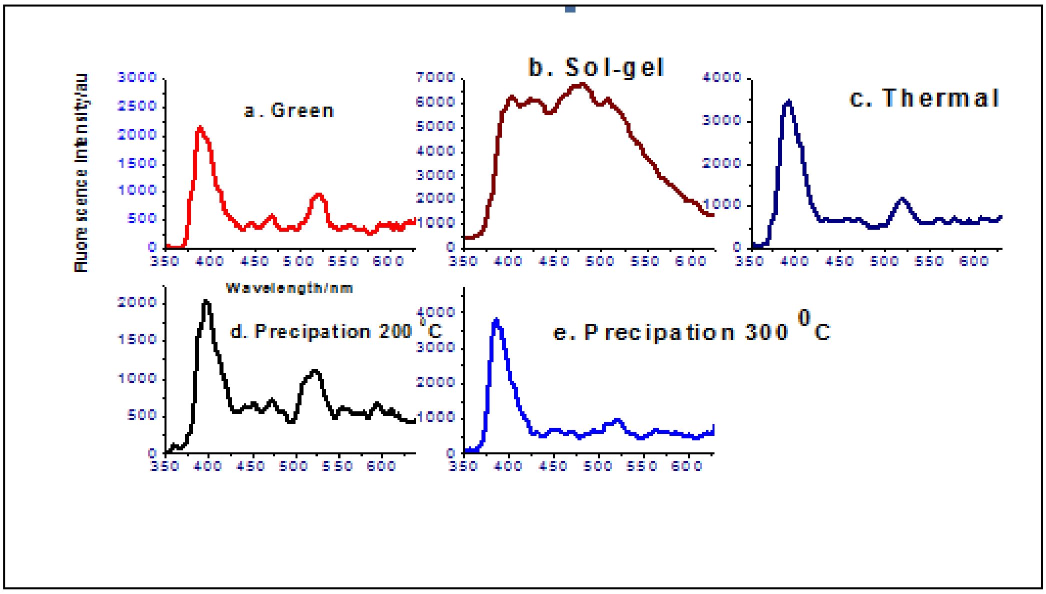

Figure 4.13: The emission spectra of ZnO NPs synthesized using a) Green Method b) Sol-gel method at 400℃ calcinations temperature c) Thermal decomposition method at 400 ^{0}C for three hours and (d, e) Precipitation method at 200℃ and 300℃ respectively

The photoluminescence spectra reveal that for all samples the green luminescence band observed in the wavelength region of 507-522 nm related to recombination of the electron in singly ionized oxygen vacancies with the photon excited holes in the valance band. The yellow band appeared in our samples at 560 and 550 nm for thermal and precipitation prepared methods are due to recombination of electron with deeply trapped holes in the in the oxygen interstitials (O_i) located at around 2.2 eV below conduction band. The orange luminescence band around 610 nm for all samples can be attributed to the transition of electron from conduction band to oxygen interstitials located at 1.34 eV above the balance band (Özgür et al., 2005).

Furthermore, The peak emission of the samples is independent of the temperature but its emission intensity depends on the temperature i.e it increased as the temperatures of the samples increased.

4.2.5 Antimicrobial activity of the ZnO nanoparticles

The antimicrobial activity of sol-gel, thermal decomposition, precipitation and green route-derived ZnO NPs suspensions of different concentrations towards various bacterial and fungal pathogens were tested by the well diffusion agar methods (Fig. 4.14). ZnO NPs synthesis using all the above methods showed antimicrobial activity against all selected test organisms but maximum activity was observed in *S. aureus* and minimum activity was in *C. albicans* (Fig. 4.14). Previously, it was reported that gram-negative bacteria and fungus seem to be more resistant to ZnO NPs than gram-positive bacteria (Zarrindokht Emami-Karvani, 2012); (S et al., 2017). The mechanisms of ZnO NPs for antimicrobials activities are due to disruption of cell membranes of bacteria and fungus probably by the production of reactive oxygen species (ROS), such as superoxide anion, hydroxyl radicals and hydroxyl ion (L. Zhang et al., 2007); (J. Zhang, 2011).

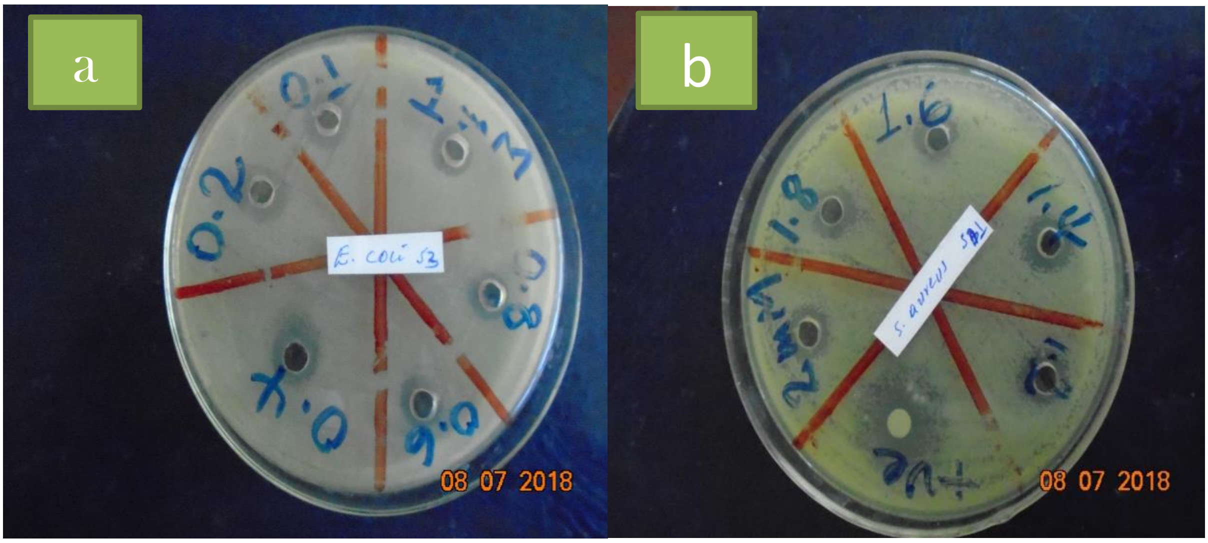

Figure 4.14: The antibacterial activity of ZnO NPs synthesized using thermal decomposition method and applied on a) *E.coli* and b) *S.aureus*

In our study, the antimicrobial activity of ZnO NPs increased with decreasing size of the crystal. It showed that smaller size particles enhanced antimicrobial activity due to the larger surface area to volume ratio. The antimicrobial activities of ZnO NPs synthesized using green method showed greater significance zone of inhibition when compared to other chemical methods due to difference in the size of NPs (Fig.4.15). The results also indicated chemically synthesized NPs with rod shape performed better antimicrobial activities than the others. Similarly, (Gunalan et al., 2012) reported that green ZNO NPs are responsible for significant higher antimicrobial activity. They suggested that green ZnO NPs could be applied effectively in agriculture and food industry.

Table 4.6: Minimum Inhibatory Concentration (MIC) values in µg/ml of ZnO NPs synthesized using different techniques.

	Minimum Inhibatory Concentration(MIC) in µg/ml of ZnO NPs synthesized using different methods per their ZOI in mm.		
Type of pathogens	Sol-gel at 400^0C	Thernal decomposition	Precipitation at 200^0C
E. coli	43.4±15	37.97±24	54.25±18
P. auruginosa	48.82±16	43.4±18	59.67±24
B. subtillis	32.55±16	37.97±24	43.40±9
S. aureus	29.83±20	21.70±9	43.40
S. typhi	54.25±9	48.82±16	70.52±12
C. albicans	92.23±9	86.80±13	119.35±33

The minimum concentration of ZnO NPs which completely inhibited the growth of bacteria and fungus were found to be in the ranges of 21-43 $\mu g / ml$, 37-70 $\mu g / ml$ and 86-119 $\mu g / ml$ for gram positive bacteria, gram negative bacteria and fungus respectively (Table4. 6). Minimum concentration of ZnO NPs (21µg/ml) was recorded in *S. aureus* by thermal decomposition method where maximum concentration was recorded in *C. albicans* by precipitation method (Table 4.6). Our results also confirm that gram-negative bacteria and fungus are inhibited at higher concentrations of ZnO NPs than gram-negative bacteria.

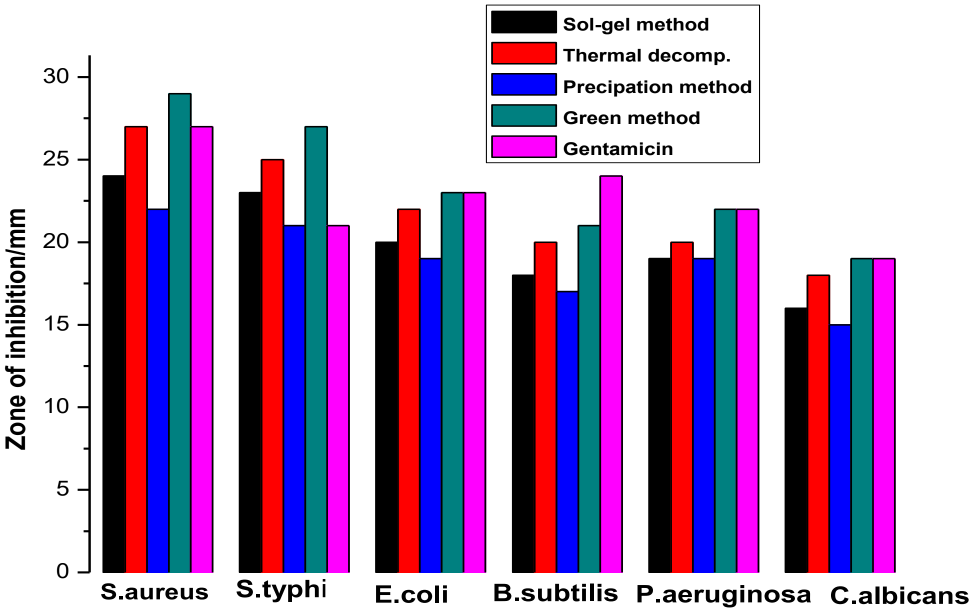

Figure4.15: The antimicrobial activities of ZnO NPs synthesis using sol-gel, thermal decomposition, precipitation, green methods and Gentamicin drug at the concentration of 1280 $\mu g / ml$

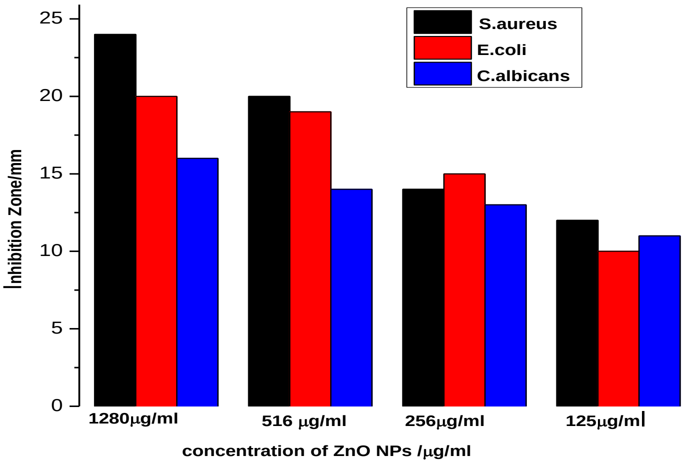

Figure 4.16: The antimicrobial activities of different concentration of ZnO NPs synthesized using sol-gel method against gram positive bacteria (*S.aureus*) gram negative bacteria (*E.coli*) and fungus (*C. albicans*)

4.3. Interaction of Caffeic Acid (CFA) with ZnO Nanoparticles (NPs) using Spectroscopic Techniques

4.3.1. Fluorescence quenching of caffeic acid by ZnO Nanoparticles

There are several techniques to study the interaction between metal oxide and biomolecules; among these the most simple and sensitive one is the fluorescence quenching method (Al-Kady et al., 2011); (Kang et al., 2004); (Boulos et al., 2013); (Iosin et al., 2009). The functional groups of the biomolecules are main contribute for the fluorescence spectra of these compounds and they are sensitive to local medium of the environment. Fig. 4.17A shows the fluorescence spectra of CFA in the presence and the absence of ZnO NPs.

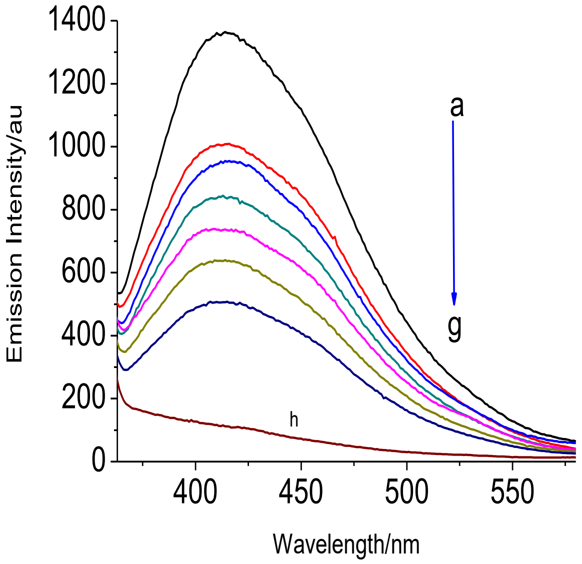

Figure 4.17A: Emission spectra of CFA (concentration =1.72x10^{-5} M) in the presence of ZnO in water at 298 K. The concentration of ZnO in a) 0, b) 7.55x10^{-6} M, c) 8.44x10^{-6} M, d) 9.56x10^{-6} M, e) 1.10x10^{-5} M, f) 1.30x10^{-5} M, g) 1.59x10^{-5} M and h) Emission spectrum of ZnO (concentration=1.59×10^{-5} M) excited at 310nm

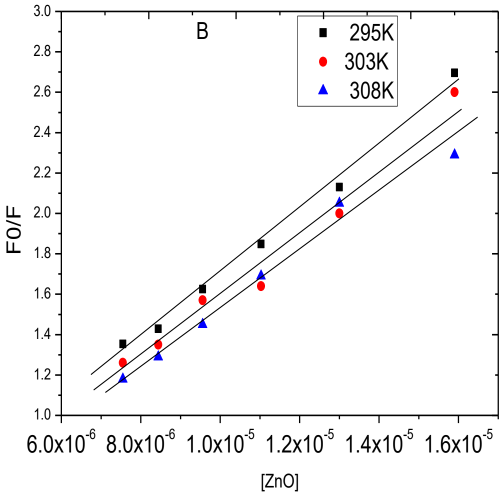

Figure 4.17B: Stern-Volmer plots for the quenching of CFA by ZnO NPs at temperature 295, 303 and 308 K

The peak fluorescence spectra of CFA were observed at 412 nm. The fluorescence intensity of CFA decreased with increasing ZnO NPs concentration without shift in the peak position of the spectra. The data indicated that ZnO NPs quenches the intrinsic fluorescence intensity of the molecule. The strong quenching effects clearly indicate the existence of the binding of the ZnO NPs with CFA molecule. It is expected that the quenching are due to CFA functional groups COOH and OH are bind to ZnO nanoparticles and result in decrease the intrinsic intensity of CFA. It also checked and observed that a ZnO fluorescence spectrum has insignificant contribution up on the spectra of CFA as shown in (Fig.4.17A). Many researchers have reported the interaction of ZnO NPs with biomolecules such as bovine serum albumin amino acid L-trpptophan (Al-Kady et al., 2011); (Kang et al., 2004), nucleic acid (Boulos et al., 2013), aminoacid (Iosin et al., 2009), by experimental and theoretical studies and they found similar effects.

4.3.2. Binding Mechanisms between CFA and ZnO NPs

Fluorescence quenching is process of decreases in the fluorescence intensity of a given substance. A variety of processes are result in quenching, such as excited state reactions, energy transfer, ground sate complex-formation and collisional quenching (Ross & Subramanian, 1981). There are two mechanisms of fluorescence quenching: dynamic and static quenching. The two quenching mechanisms can be identified by the different trends of excited sate lifetime fluctuation with the temperature rising (Ross & Subramanian, 1981).

The quenching constant decreases with increasing temperature for static quenching, but it is increases with increasing temperature for dynamic since higher temperature result in a large diffusion coefficient. Similarly, higher temperature is likely to result in decreases the stability of the complex and thus lower the values of static quenching constant.

In order to interpret the quenching mechanism of CFA by ZnO NPs the fluorescence quenching constant (K_{sv}) analyzed according to the well-known Stern-Volmer equation (5.1)

$$\frac{F_0}{F} = 1 + K_q \tau_0 [Q] = 1 + K_{sv}[Q] \qquad (5.1)$$

where, F_0 and F are the steady sate fluorescence intensities in the absence and presence of the quencher respectively; [Q] is the concentration of ZnO nanoparticles; K_{sv} is the dynamic quenching constant; K_q is the quenching rate constant, $K_{sv} = K_q \tau_0$; τ_0 is the fluorescence lifetime of CFA in the absence of ZnO nanoparticles. The K_{sv} was determined by linear regression of Stern-Volmer equation. Fig 2B is the Stern-Volmer plots for the quenching of CFA by ZnO nanoparticles at different temperatures. The plots are linear and the slope decreases with increasing temperature, which indicates that the quenching process rationalized in terms of static quenching mechanism rather than dynamic. Moreover, considering the fluorescence lifetime τ_0 of CFA 1ns as reported by (Morales et al., 2005), the rate of quenching constant K_q determined for three different temperatures and the values are given in Table 4.7.

Table 4.7: Stern-Volmer constant, quenching rate constant for the interaction of CFA with ZnO nanoparticles at different temperatures.

T(K)	K_{sv}(Lmol^{-1})	K_q(Lmol^{-1}s^{-1})	R
295	1.84x10^{5}	1.84x10^{14}	0.99
303	1.61x10^{5}	1.61x10^{14}	0.99
308	1.40x10^{5}	1.40x10^{14}	0.99

The obtained K_q values are in the ranges of (1.4-1.84)10^{14} L mol s^{-}1 for CFA. The values are exceed by far the diffusion controlled rate constant in aqueous solution, that mean 2.0x10^{10} L Mol^{-1} s^{-1} , confirming that the quenching does not involve the dynamic diffusion process but occurs due to formation of the complexes of CFA-ZnO. Moreover, in all temperatures the plots exhibit good linear relationship indicates the domination of static quenching mechanisms in the studied concentrations. The obtained quenching constant are similar with the results obtained for the fluorescence quenching of bovine serum albumin by Al_2O_3 NPs (Morales et al., 2005) and ZnO NPs (Al-Kady et al., 2011) but smaller than the result reported by (Mohd Omar et al., 2014) for the interaction of iron oxide NPs with coumarin.

4.3.3. Binding constant and binding sites

When molecules are bound independently to a set of equivalent sites on macromolecules, the equilibrium between free and bound molecules is given (Kang et al., 2004) by Eq. (5.2)

$$Log\left(\frac{F_0 - F}{F}\right) = LogK_a + nLog[CF] \qquad (5.2)$$

Where K_a is the binding constant of ZnO NPs with CFA, and n is the number of binding sites per CFA molecule. The values of K_a and n were determined from the slope and intercept of the linear fit of Eq. (4.2) to the experimental data. The values of the binding constant of ZnO NPs with CFA at 296, 303 and 308 K are listed in Table 4.8. The values of binding constants are decreased with the increasing temperature indicates the formation of unstable compound; partly decompose at relatively higher temperatures. The binding site numbers n are about 2 indicating that there are two sites for the binding of ZnO to caffeic acid.

Table 4.8: Binding constants K, and binding site n of CFA-ZnO complex at different temperatures (CFA concentration 1.72x10-5 M)

T(K)	log K	K($Lmol^{-1}$)	n	R
295	12.06	11.47×10^{11}	2.46	0.99
303	11.70	4.99×10^{11}	2.39	0.99
308	11.53	3.42×10^{11}	2.37	0.99

Strong binding constants were obtained between ZnO NPs and CFA and the values are by far much higher than the binding observed between biomolecules. From experimental results observation it could be inferred that CFA have high binding affinities with NPs than other biomolecules such as BSA (Mandal et al., 2009). On the other hand the results are quite similar with recently reported for the binding of Gold metal nanoparticles with bovine serum albumin (Boulos et al., 2013); (Iosin et al., 2009).

4.3.4. Thermodynamic parameters and nature of the binding forces

The formation of binding can be described by several biophysical parameters such as association constant, and other thermodynamic properties. To obtain further insight into the weak interactions associated with the complexation of ZnO NPs with CFA, we endeavored to determine the thermodynamic parameters using Van't hoff equation. If the enthalpy change (ΔH) does not significantly vary over the temperature ranges of study, then the thermodynamic parameters can be determined by Van't Hoff Eq. (5.3)

$$\ln K_a = -\frac{\Delta H}{RT} + \frac{\Delta S}{R} \tag{5.3}$$

The free energy change ((ΔG) can be calculated at each temperature using Eq. (5.4)

$$\Delta G = -RT \ln K_a = \Delta H - T\Delta S \tag{5.4}$$

Where, K_a is the binding constant at the corresponding temperature, R is the gas constant, T is the experimental temperature. From the linear relationship between $\ln(K_a)$ and reciprocal of absolute temperature, the values of thermodynamic parameters are obtained and listed in Table 4.9.

Table 4.9: Thermodynamic properties determined by fluorescence quenching of CFA by ZnO nanoparticle

T(K)	$\Delta G\ (kJmol^{-1})$	$\Delta H\ (kJmol^{-1})$	$\Delta S (Jmol^{-1}K^{-1})$
295	-67.97	-70.89	-9.99
303	-66.28	-	-
308	- 67.80	-	-

The sign and magnitude of the thermodynamic parameters associated with various individual types of interaction were characterized by (Ross & Subramanian, 1981). The results obtained from fitting of Eq. (5.3) to the experimental results are negative ΔH , and ΔS indicate that hydrogen bonds and van der Waals forces played a major role in the reaction between ZnO NPs and CFA, while the negative sign for ΔG indicates the spontaneity of the binding for ZnO with CFA. The obtained results are also similar with the report of (Mandal et al., 2009) studied for the interaction of ZnO NPs with bovine serum albumin which involves hydrogen bonds and van der Waals forces.

4.3.5. Energy transfer between ZnO NPs and caffeic acid

Fluorescence Resonance Energy Transfer describes the mechanism of energy transfer between two light-sensitive molecules or chromophores. A donor chromophore, initially in its electronic excited state, may transfer energy to an acceptor chromophore through nonradiative dipole–dipole coupling. The Forster theory shows that energy transfer affected not only by the distance between the acceptor and donor, but also by the critical distance of the energy transfer (R_0), which can be calculated by using the following Eq. (5.5)

$$E = 1 - \frac{F_0}{F} = \frac{R_0^{\ 6}}{R_0^{\ 6} + r^6} \tag{5.5}$$

In this cause, E is the energy transfer efficiency, F and F_0 are the fluorescence intensities of fluorophore in the presence and absence of quencher, r is the donor-acceptor distance and R_0 is the critical distance when the energy transfer efficiency is 50 % and its value is calculated by Eq (5.6)

$$R_0^{\ 6} = 8.8x10^{-25} K^2 \ N^{-4} \phi_D J \tag{5.6}$$

the K^2 is the orientation factor related to the geometry of the donor and acceptor of the dipoles, N is the average refractive index of the medium, ϕ_D the fluorescence quantum yield of donor and J is the effect of spectral overlap between the emission spectrum of the donor and the absorption spectrum of the acceptor which can be calculated using Eq. (5.7)

$$J = \int_0^\infty F(\lambda)\varepsilon(\lambda)\lambda^4 d\lambda \Big/ \int_0^\infty F(\lambda) d\lambda \tag{5.7}$$

where the fluorescence intensity of the donor in the wavelength region of λ to $\Delta\lambda$ and ε the molar extinction coefficient of the acceptor in the wavelength region of λ to $\Delta\lambda$. Fig. 4.18A shows the overlap of UV-Vis absorption spectrum of ZnO NPs and the fluorescence emission of spectrum of caffeic acid.

In the above Eqs. (4.5-4.7) K^2= 2/3 and N=1.33 and ϕ_D is the quantum efficiency of the donor. The calculated results are E= 68.38 %, J= $2x10^{-16}$ Lcm^3, R_0 =3.15 nm, r= 2.87 nm, and ϕ_D = 0.0265 respectively. The average distance between the donor (CFA) and acceptor (ZnO NPs) are in the ranges of 2-8 nm scale, indicates that the energy transfer from the CFA to ZnO NPs occurred with high probability. Furthermore, the binding distance is shorter than 7 nm and $0.5R_0 < r < 2R_0$ is well condition required for applying Forster's non-radative energy transfer theory. The study results revealed that ZnO NPs could strongly quench the intrinsic fluorescence of the CFA by static quenching.

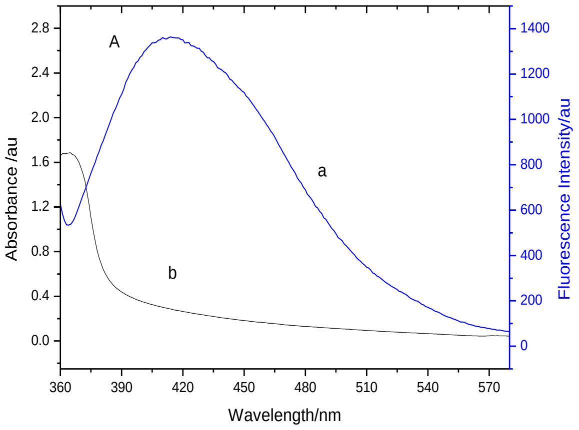

Figure 4.18A: The overlap of the emission spectrum of CFA a) and absorption spectrum of ZnO nanoparticle b)

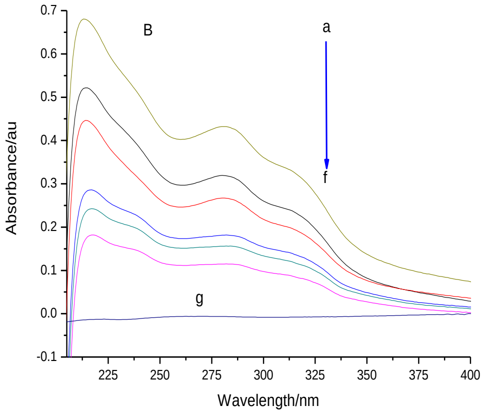

Figure 4.18B: UV-vis absorption spectra of CFA (Concentration $=5.22\text{x}10^{-5}$ M) in the presence of ZnO at T= 296 K in water. The concentration of ZnO in a) 0, b) $7.55\text{x}10^{-6}$ M, c) $9.56\text{x}10^{-6}$ M, d) $1.10\text{x}10^{-5}$ M, e) $1.30\text{x}10^{-5}$ M, f) $1.59\text{x}10^{-5}$ M. and g) UV-Vis absorption spectrum of ZnO (concentration=$1.59\text{x}10^{-5}$ M)

4.3.6. UV-Vis Absorption Spectrscopy

Fig.4.18B shows the absorption spectra of CFA in the absence and prescence of ZnO nanoparticles at different concentrations. In the presence of colloidial ZnO nanoparticles the absorbance of CFA undergoes hypochromic effects, slightly red shift and a broadening of the absorption band were observed as the concentration increases. The effcts indicatees while adding colloidal nanoparticles to the solution of CFA it gets adsorbed on the surface of ZnO particles and involves the formation of ground state complex of the type of non-covalent bonding. The absorption maximum of molecules with some functional groups strongly depend on medium polarity and dielectric constant. It is likely that the CFA…ZnO having less molar extinction coeffcients than the unadsorbed state, may be factor for the decrease in the absorbance of CFA in the presence of ZnO nanoparticles. The effects will confirm the adsorption of CFA on ZnO nanoparticles also the good evidence that the fluorescence quenching of the CFAc induced by ZnO are mainly caused by static quenching.

4.3.7. Fourier Transform Infrared (FT-IR) Spectroscopy

Fig 4.19A shows the vibrational spectra of CFA and its corresponding CFA-ZnO. The vibrational spectra of CFA are mainly characterized by hydroxyl and carbonyl functional groups. The two parallel peaks located at 1200-1270 cm^{-1} due to vibration of O-H group attached to benzene ring and the other absorption band peaked in the regions of 1600-1700 cm^{-1} from C=O stretching (Coates, 2006); (Gunasekaran et al., 2005). In addition strong and isolated peak located at 1447 cm^{-1} are due to C=C-C aromatic ring stretching. On the other hand, on the spectra of CFA-ZnO, the main peaks weren't existed due to adsorption CFA on the surface of colloidal ZnO nanoparticles. This is also another conformation for the interaction of CFA and ZnO nanoparticles.

4.3.8. Dynamic Light Scattering (DLS) analysis

The effects of CFA on the mean hydrodynamic diameter (MHD) of different concentration of ZnO NPs were investigated and shown in Fig 4. 19B. It was noticed that the size of ZnO NPs was increased when CFA introduced in to the system. The MHD value of C= $7.55x10^{-6}$ M ZnO NPs was 295 nm. Upon addition of CFA the mean size increased to 396 and 955 nm for ZnO NPs C= $7.55x10^{-6}$ and $1.30x10^{-5}$ M respectively. The increased MHD size of ZnO might be due to aggregation of CFA over the NPs leading to the CFA-ZnO complex forms. Similar effects were also recently observed and reported elsewhere for the interaction of BSA with Al_2O_3 NPs.

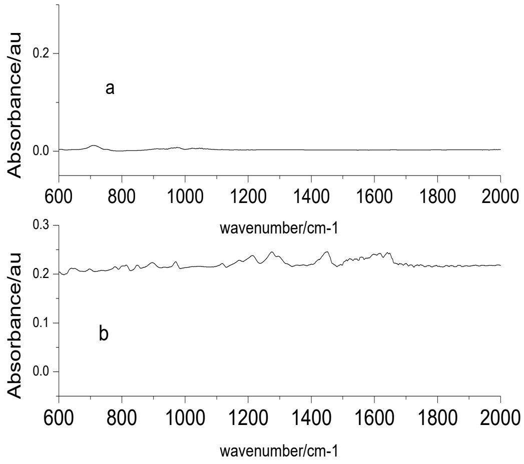

Figure 4.19A: FTIR spectra of a) CFA-ZnO and b) CF

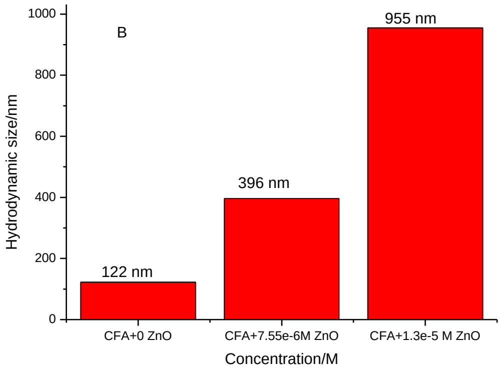

Figure 4.19B: Hydrodynamic size of CFA in the absence and presence of ZnO NPs

4.3.9. Transmission Electron Microscopy Measurement

To study further insight on the interaction of ZnO NPs and CFA the solutions were also monitored under TEM. Fig 4.20(a-b) shows the TEM images of ZnO NPs and its corresponding CFA-ZnO NPs. In Fig 4.20(a) the TEM images of ZnO NPs are fully aggregated and spherical in shape. The estimated average size of the particle is about 30 nm. On the other hand, in Fig 4.20(b) disaggregation of ZnO NPs and adsorption of CFA on the surface was noticed which expected to alter the typical environment of NPs. Adsorption of negatively charged CFA onto ZnO NPs makes the surface negatively charged and probably result in repulsion between nanoparticles and leading to dispersion of the already aggregated nanoparticles. Furthermore, stable suspension was also noticed in the presence of caffeic acid. Recently similar observations were reported by (Mohd Omar et al., 2014) on the interactive process and stability of ZnO NPs in the presence of humic acid substances. Such kind of information, on the physical and chemical aspects of NPS behaviors in biological system is important in the future of nano-medical application

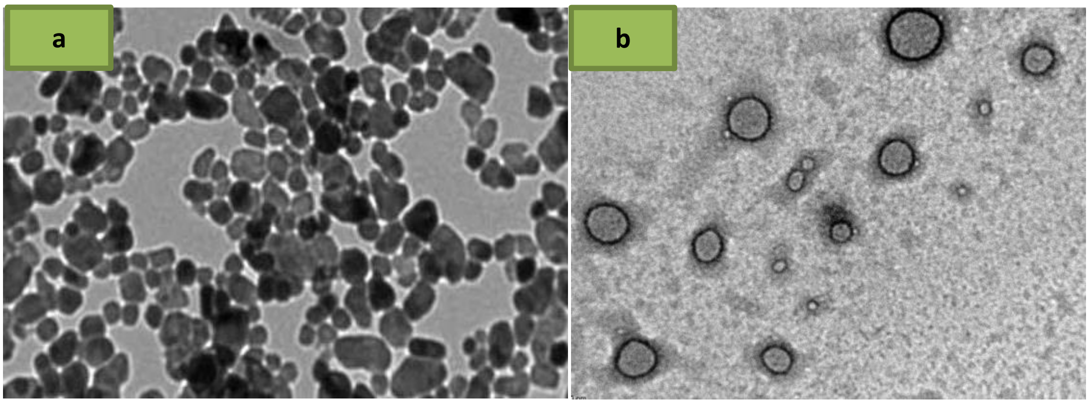

Figure 4.20: TEM image at 100nm of a) ZnO NPs and b) CFA-ZnO NPs

4.4. Incorporation of Zinc oxide nanoparticles in cotton textiles for Ultraviolet light protection and antibacterial activities

4.4.1. X-ray diffraction Analysis

Figure 1a and b show the XRD pattern of ZnO nanoparticles synthesized using water (S-1) and 1, 2-ethanediol (CH_2OHCH_2OH) (S-2) solvent respectively. All diffraction peaks are in a good agreement with wurtzite structure (hexagonal phase, space group $P6_{3mc}$) with lattice parameters a=b= 3.249 A^0 and c= 5.206 A^0 as reported in (JCPDS card no. 36-1451). The nine characteristic peaks appeared at 31.802, 34.468, 36.306, 47.600, 56.592, 62.951, 66.411, 67.91 69.152 correspond to (100), (002), (101), (102), (110), (103), (200), (112) and (201) of crystal planes. The samples (101) peak is the most intense peak that shows the plane is a preferred growth plane (Belay et al., 2019). The average crystallite size of the ZnO NPs calculated using Debye Scherer formula Eq. (2.8) were 32 and 26 nm for S-1 and S-2 respectively.

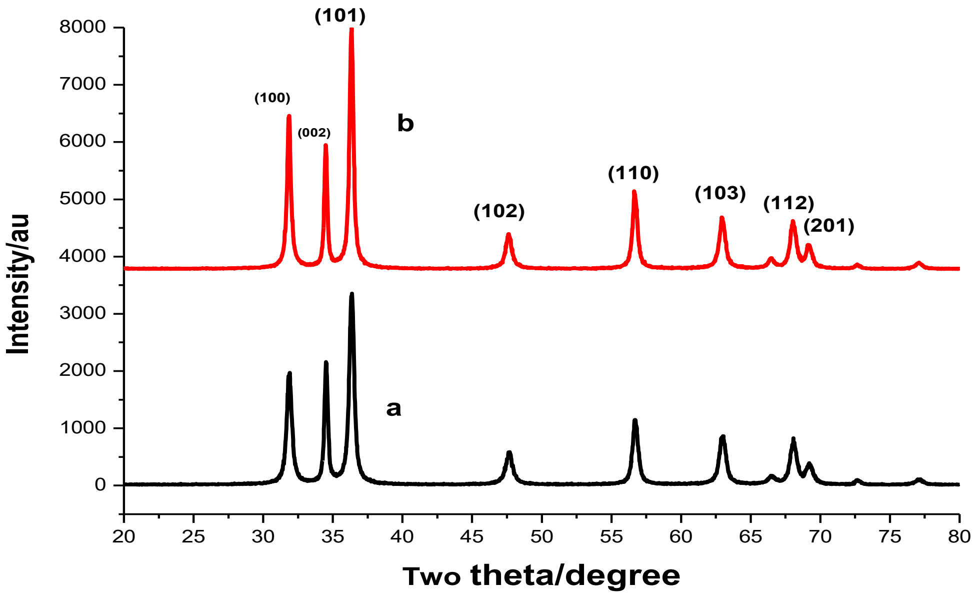

Figure 4.21: XRD patterns of ZnO NPs synthesized using a) precipitation method in water reaction medium and b) precipitation method in 1,2- ethanediol reaction medium respectively

4.4.2. Scanning Electron Microscopy (SEM) Analysis

Figure 4.22(a) shows the SEM images of uncoated cotton fabrics whereas, Figure 4.22(b-e) shows the SEM images of cotton fabrics treated by ZnO NPs synthesized using S-1, S-2 and *in situ* methods respectively. The SEM images analysis confirmed uniform and dense depositions of ZnO NPs available on the surface of cotton fabric. The morphology of ZnO NPs revealed that nanostructures were homogeneously formed on the fabric' surface for S-1 and S-2 with some agglomerated nanoparticles in Figure 4.22(b-c). The morphology of ZnO NPs synthesized using these methods have spherical shape, on the other hand ZnO NPs synthesized using *in situ* method have bundle/flower-like shape structures. Bundle like particles are composed of few rods adhered together with different forms, whereas the flower like particles consist many single rods aligned in a radial way from the center (Shateri-Khalilabad & Yazdanshenas, 2013). The particles size and shape play a primary role in determining their adhesion to the fibers (Becheri et al., 2008); (Broasca et al., 2013). Larger particles sizes and agglomerates NPs can easily be removed from the fibre surface, while smaller particle will penetrate deeper and adhere strongly into the fibre matrix.

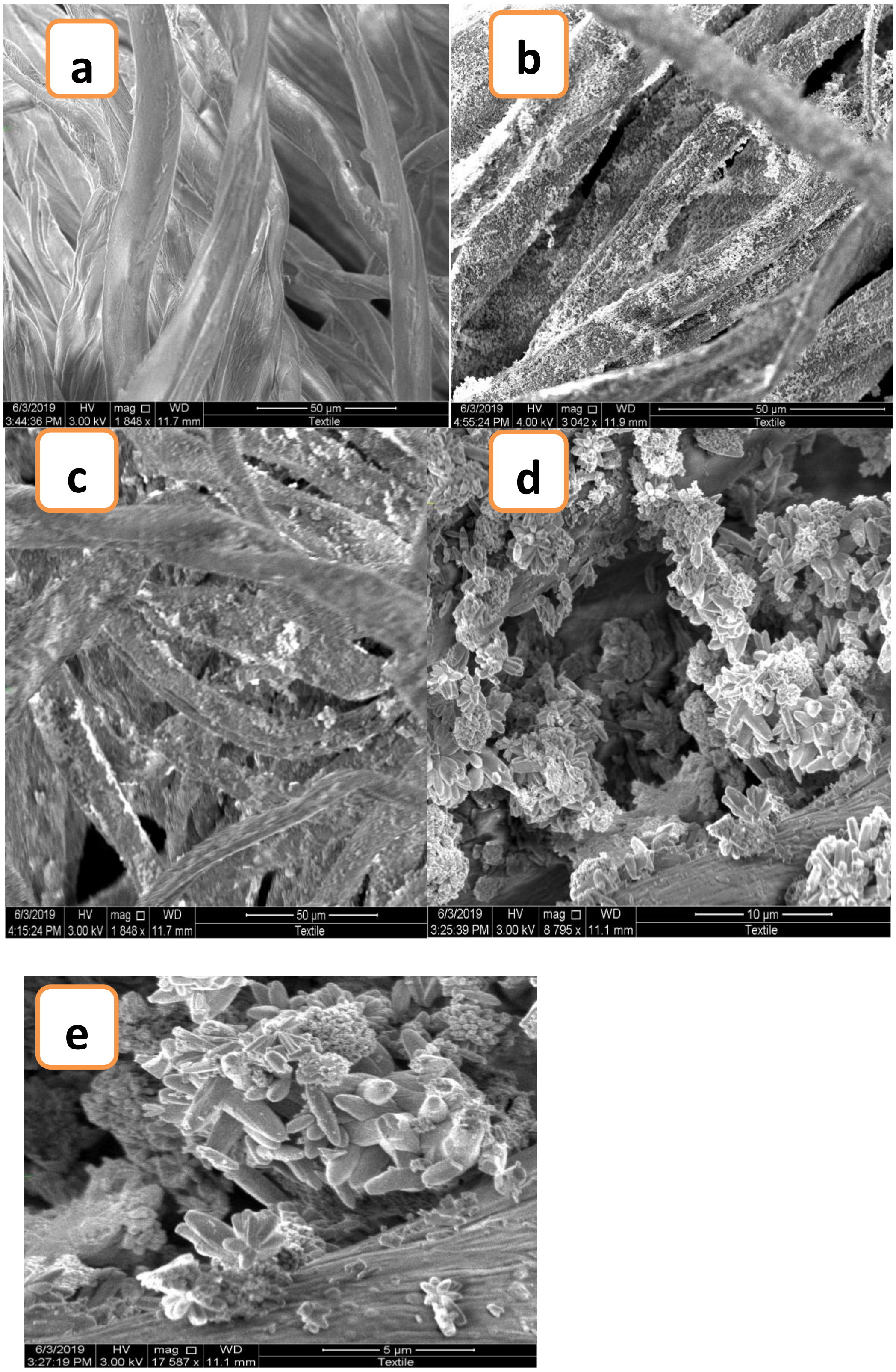

Figure 4.22: SEM of a) uncoated cotton textiles, b) cotton textiles coated with ZnO NPs synthesized using precipitation in water medium c) cotton textiles coated with ZnO NPs synthesized using precipitation in 1,2- ethanediol medium and (d & e) cotton textiles coated by ZnO NPs synthesized using *in situ* method

4.4.3. UV light protection of cotton textiles

The solar UV radiation is composed of UV-A (315-400 nm), UV-B (290 -315nm) and UV-C (200-290nm). UV transmittance through a fabric is the decisive factor in determining the UV protection factor of the cotton fabrics. The incorporation of ZnO NPS on the cotton fabrics increases the absorption of UV light as shown in the UV absorption spectra of untreated and treated fabrics of cotton textiles in Figure 4.23(**a-f**). The untreated cotton fabrics have low UV radiation absorbance (Fig. 4.23 **a** and **d**) as compared to the cotton treated with ZnO NPs (Fig. 4.23 **b,c** &**f**). The application of nanosized ZnO NPs on the cotton fabric increases the absorption of UV light over the entire investigated spectrum as compared to untreated samples. Our results indicated, higher UV absorbance was obtained when ZnO NPs applied on cotton samples by *in situ* method as compared to others as shown in Figure 4. 23 **c** and **e**. This implies the dependence of UV light protection of on the shape of NPs and precursor chemicals. It has been previously reported that the shape of ZnO NPs synthesized from $ZnCl_2$ precursor has rod shape and maximum peak of absorbance in the UV-B regions as compared to others (S et al., 2017). Recent report demonstrated that the shapes of nanoparticle greatly affected the multifunctional properties of textile fabrics especially those coated with ZnO-NPs. Nano-rod ZnO NPs has more antibacterial properties against pathogenic bacteria and UV protection index compared to the hexagonal ZnO-NPs (Fouda et al., 2018); (Mohamed et al., 2019). Our study results also indicated that the UV absorbance ability of cotton factory products are higher than the local product as shown in Fig. 4.23 **b** and **c** versus Fig.4.23 **e** & **f**. This difference may be due to structure of fabric and initial treatment of fabrics with additive chemicals (Sirelkhatim et al., 2015).

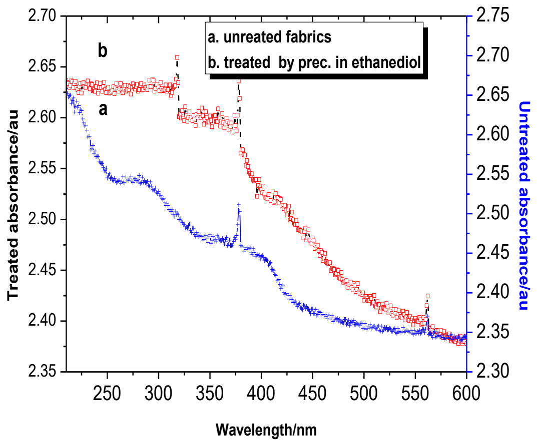

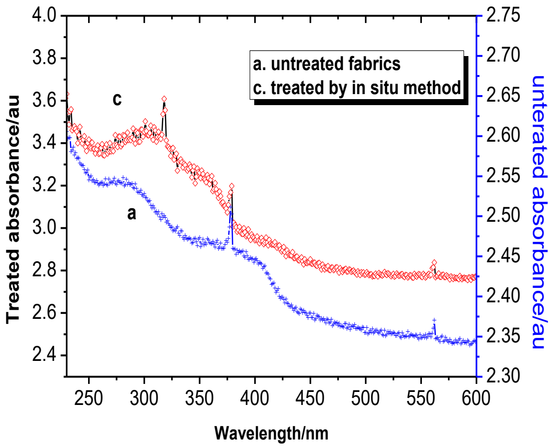

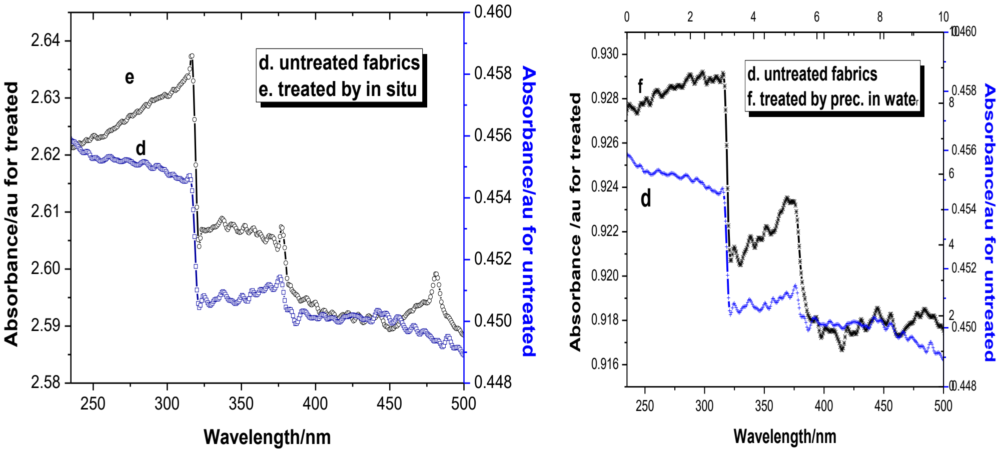

Figure 4.23: UV-Vis absorption spectra of of a) uncoated cotton textiles (factory product), b) cotton textiles (factory product) coated with ZnO NPs synthesized using precipitation in 1,2-ethanediol medium c) cotton textiles (factory product) coated by ZnO NPs synthesized using in situ method d) uncoated cotton textiles (local product) e) cotton textiles (local product) coated by ZnO NPs synthesized using *in situ* method f) cotton textiles (local product) coated with ZnO NPs synthesized using precipitation in water medium

Ultraviolet protection factor and percentage of UV transmission for UV-A and UV-B ranges were calculated using Eq. (2.15) and presented in Table 4.10. Higher UPF value means the ability to protect UV radiation. The highest UPF 320 were obtained on fabric cotton synthesized using an *in situ* method on factory products. Similarly, the UPF factor obtained for locally product was 44.6 using the same method. On the other hand, small amounts UPF obtained for untreated cotton. The UPF obtained in this research is by far much higher than the result previously reported by other co-workers (Becheri et al., 2008); (Broasca et al., 2013). The fabric with an UPF of >40 is considered to provide excellent protection against UV radiation and considered as totally safe sun-blocks. The UPF value <15 indicates no protection against transmittance of UV radiation through fabric (Louris et al., 2018); (Grifoni et al., 2009). The UV radiation transmitted ability calculated using Eq. (2.15) of the ZnO NPs coated cotton has also been very small as compared to the untreated cotton as shown table 4.10. The factory product of fibre cotton has also less UV light transmission as compared to the local cotton which may be due to the difference in their fabric structure and initial treatment of fabrics with additive chemicals (Sirelkhatim et al., 2015). Furthermore, the effects of washing fabrics on UPF were evaluated by washing the fabrics two times and the results demonstrated that washing has no effects on the UPF and

UV transmission ability. The observation is consistent with the results of previous works reported elsewhere (Shateri-Khalilabad & Yazdanshenas, 2013).

Table4.10: UPF and percentage of UV transmission of factory cotton and local cotton fabrics coated by ZnO NPs.

Sample	**UPF**		**UV transmission %**		
	UV-A	**UV-B**	**UV-A**	**UV-B**	**UV-A/UV-B**
Fabric Cotton					
Untreated	17.6	19	5.9	5.4	1.1
Synthesis 1	118	209	0.9	0.8	1.13
Synthesis 2	196	213	0.26	0.215	1.21
In situ	226	320	0.067	0.0371	1.8
Local Cotton					
Untreated	2.85	2.97	35	34.6	1.01
Synthesis 1	8.5	10.7	12	11.8	1.01
Synthesis 2	12.83	15.28	7.8	7.6	1.02
In situ	42.7	44.6	0.24	0.23	1.04

4.4.4. Antibacterial activity of the ZnO nanoparticles

Figure 4.24 (a-d) shows the antibacterial activity of ZnO nanoparticles synthesized using S-1 and *in situ* methods on *E. coli* and *S. aureus* bacteria respectively. The antibacterial activity showed that ZnO nanoparticle synthesized using *in situ* method (Fig. 4.24(c-d) has exhibited strong antibacterial activity against gram positive (*S.aureus)* and gram negative (*E.coli)* bacteria as compared to the S-1 method (Fig. 4.24 (a-b). This may be due to the difference in the shape and size of ZnO NPs applied on the cotton fabrics (Mohamed et al., 2019); (Salahuddin et al., 2015). It was also observed that ZnO nanoparticles have better antibacterial activity on *gram-positive* (*S. aureus*) than the *gram-negative* (*E. coli*) bacteria. We found that the antibacterial activity is dependent on the concentration of ZnO NPs as shown in Figure 4.24. Generally the growth of the inhibition zone of *E. coli* and *S. aureus* has been increased as the concentration of ZnO nanoparticles increased as shown on the discs also. The mechanisms of ZnO NPs for antimicrobials are due to disruption of cell membranes of bacteria and fungus probably by the production of reactive oxygen species (ROS), such as superoxide anion, hydroxyl radicals and hydroxyl ion (L. Zhang et al., 2007); (Sirelkhatim et al., 2015).

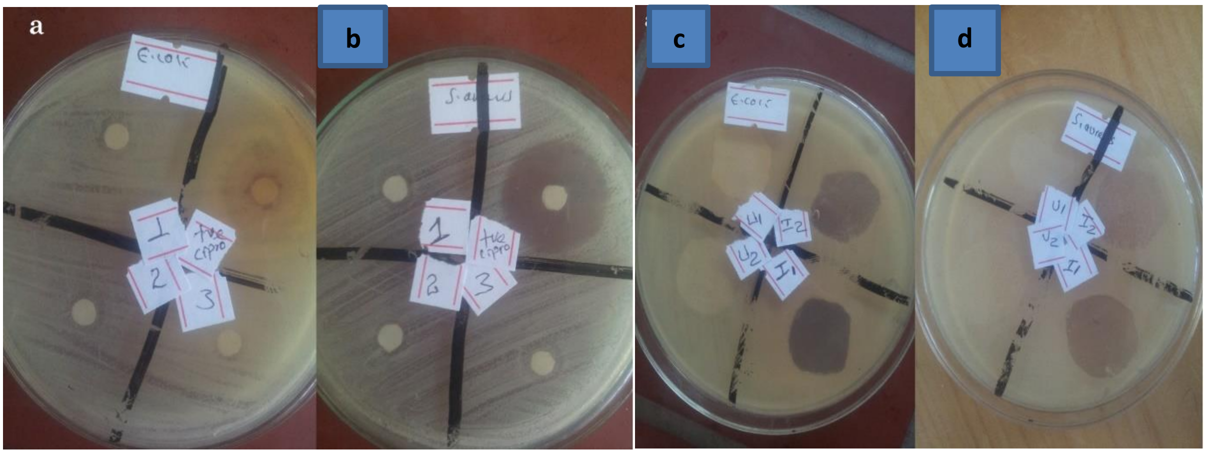

Figure 4.24: Shows the antibacterial activities of ZnO NPs with different concentrations applied on. *E. coli*, and *S. aureus* synthesized using precipitation method in water medium (a,b) and synthesized using *in situ method* (c,d)

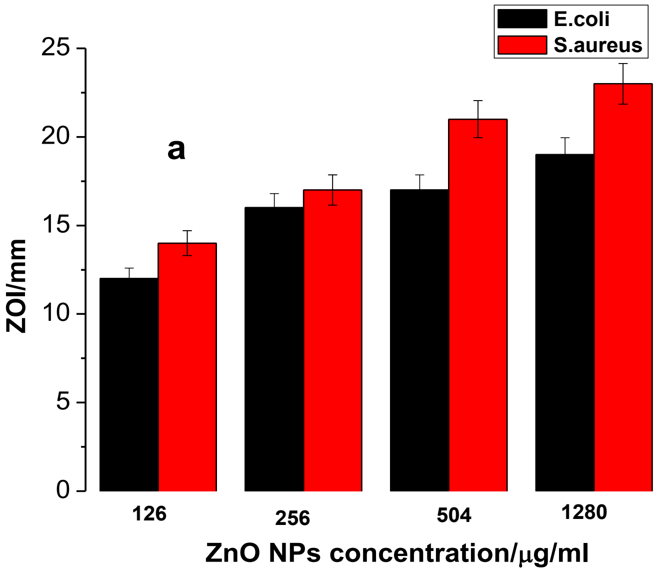

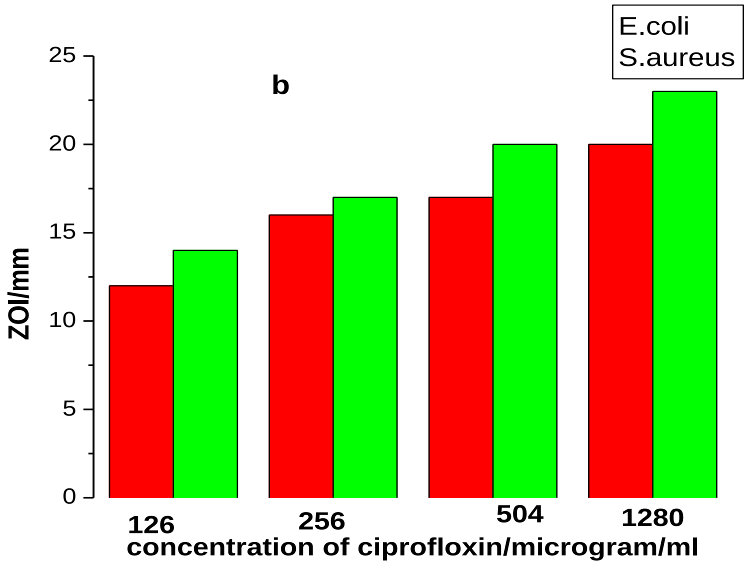

Figure 4.25: The antibacterial activities applied against *S. aureus* and *E. coli* at different concentrations a) ZnO NPs synthesized using precipitation method in water medium b) The standard antibiotic drug ciprofloxacin.

5. Conclusions

Zinc oxide nanoparticles were synthesized via sol-gel methods at various temperatures and PVA concentrations. The prepared ZnO NPs were characterized by different spectroscopic techniques. The XRD and SEM images of ZnO NPs indicated increment in the particle size of as annealing temperature and PVA concentration increased. The reduction in the FWHM with increasing temperature has confirmed the improved in crystallinity of the samples. The hexagonal wurtzite structure of ZnO was also confirmed from the diffraction pattern of the samples. From FTIR studies, with increasing annealing temperature, the presence of functional groups impurities was reduced as the particle size increased. The UV-Vis absorption peaks of the samples shifted towards higher wavelength (red shift) as the temperatures and PVA concentration increased. The emission spectra of ZnO NPs showed two peaks in ultra-violet and visible regions. The peak emission of the samples is independent of the temperature but its emission intensity depends on the temperature i.e. it increased as the temperatures of the samples increased.

Additionally, Zinc oxide nanoparticles were synthesized by different methods, ranging from chemical, thermal to green routes, and the efficacy of their antimicrobial activities were investigated and compared. The synthesized NPs were characterized using XRD, SEM, DLS, UV-Vis and fluorescence spectroscopy. The results of this study revealed that the antimicrobial activity of ZnO NPs increased with decreasing size of the crystal. Also, the results indicated that the gram positive bacteria were more sensitive to ZnO NPs than gram negative bacteria and fungus. In overall, it was also found that the antimicrobial activity of ZnO NPs synthesized using green method were more effective than the chemical methods due to the differences in the size of NPs.

The other work indicated the ZnO NPs have quenched the fluorophore of CFA by forming nthe ground sate complex or the formations of non-fluorescent CFA-ZnO with high binding affinities. The thermodynamic parameters determined using Van’t Hoff equation indicated binding occurs spontaneously involving the hydrogen bond and Vander Walls forces played the major role in the reaction of ZnO NPs with CFA. The FTIR, TEM and DLS measurements were also indicated the differences in the structural, morphological and sizes of CFA and ZnO NPs and their corresponding CFA-ZnO. The current finding may provide more information on the biocompatibility of ZnO NPs for the application of biological systems.

Finally, the ZnO NPs were synthesized using three different methods and applied for ultraviolet light protection and antibacterial activities. ZnO NPs synthesized by preciptation method through homogeneous phase reaction using zinc chloride as a precursor with sodium hydroxide at high temprature in water and 1,2- ethanediol at 90℃ and 150℃ respectively. The other method was in situ synthesized of ZnO NPs on the surface of cotton textiles via a simple wet chemical route.The morphology of ZnO NPs characterized by SEM on cotton fibre shows bundle or flowers shape for ZnO synthesized using *in situ method* and spherical for those synthesized using S-1 and S-2 methods. The UV protection ability of ZnO NPs coated on textiles was investigated by measuring the ultraviolet protection factor in the ranges of 280-400 nm. Higher values of UPF were obtained when ZnO NPs prepared using in situ method. The antibacterial activities of ZnO synthesized by the two methods possess very good bacteriostatic activity against *S. aureus* and *E. coli* bacteria as demonstrated by zone of inhibition.

References

Abdul Salam, H., Sivaraj, R., & Venckatesh, R. (2014). Green synthesis and characterization of zinc oxide nanoparticles from Ocimum basilicum L. var. purpurascens Benth.-Lamiaceae leaf extract. *Materials Letters*, *131*, 16–18. https://doi.org/10.1016/j.matlet.2014.05.033

Ahmed, D., Osman, M., & Mustafa, M. A. (2015). *Synthesis and Characterization of Zinc Oxide Nanoparticles using Zinc Acetate Dihydrate and Sodium Hydroxide*. *1*(4), 248–251.

Ahmed, M. T., Sarhan, A., & Hassan, A. (2016). *Preparation and Characterization of ZnO Nanoparticles by Simple Precipitation Method*. *4*(3), 507–512.

Al-Kady, A. S., Gaber, M., Hussein, M. M., & Ebeid, E. Z. M. (2011). Structural and fluorescence quenching characterization of hematite nanoparticles. *Spectrochimica Acta - Part A: Molecular and Biomolecular Spectroscopy*, *83*(1), 398–405. https://doi.org/10.1016/j.saa.2011.08.052

Alibe, I. M., Matori, K. A., Saion, E., Ali, A. M., & Zaid, M. H. M. (2017). The influence of calcination temperature on structural and optical properties of ZnO nanoparticles via simple polymer synthesis route. *Science of Sintering*, *49*(3), 263–275. https://doi.org/10.2298/SOS1703263A

Awwad, A. M., Albiss, B., & Ahmad, A. L. (2014). Green synthesis, characterization and optical properties of zinc oxide nanosheets using Olea europea leaf extract. *Advanced Materials Letters*, *5*(9), 520–524. https://doi.org/10.5185/amlett.2014.5575

Badreddine, K., Kazah, I., Rekaby, M., & Awad, R. (2018). Structural, morphological, optical, and room temperature magnetic characterization on pure and Sm-Doped ZnO nanoparticles. *Journal of Nanomaterials*, *2018*. https://doi.org/10.1155/2018/7096195

Bahnemann, D. W., Kormann, C., & Hoffmann, M. R. (1987). Preparation and characterization of quantum size zinc oxide: A detailed spectroscopic study. *Journal of Physical Chemistry*, *91*(14), 3789–3798. https://doi.org/10.1021/j100298a015

Becheri, A., Dürr, M., Lo Nostro, P., & Baglioni, P. (2008). Synthesis and characterization of zinc oxide nanoparticles: Application to textiles as UV-absorbers. *Journal of Nanoparticle Research*, *10*(4), 679–689. https://doi.org/10.1007/s11051-007-9318-3

Belay, A., Bekele, B., & Chandra Reddy, A. R. (2019). Effects of temperature and polyvinyl alcohol concentrations in the synthesis of zinc oxide nanoparticles. *Digest Journal of Nanomaterials and Biostructures*, *14*(1), 51–60.

Belay, A., Kim, H. K., & Hwang, Y. H. (2016). Probing the interaction of caffeic acid with ZnO nanoparticles. *Luminescence, 31*(3), 654–659. https://doi.org/10.1002/bio.3007

Boulos, S. P., Davis, T. A., Yang, J. A., Lohse, S. E., Alkilany, A. M., Holland, L. A., & Murphy, C. J. (2013). Nanoparticle-protein interactions: A thermodynamic and kinetic study of the adsorption of bovine serum albumin to gold nanoparticle surfaces. *Langmuir*, *29*(48), 14984–14996. https://doi.org/10.1021/la402920f

Broasca, G., Borcia, G., Dumitrascu, N., & Vrinceanu, N. (2013). Characterization of ZnO coated polyester fabrics for UV protection. *Applied Surface Science*, *279*, 272–278. https://doi.org/10.1016/j.apsusc.2013.04.084

Bunaciu, A. A., & Aboul-enein, H. Y. (2015). *X-Ray Diffraction : Instrumentation and Applications Critical Reviews in Analytical Chemistry X-Ray Diffraction : Instrumentation and Applications*. *May*. https://doi.org/10.1080/10408347.2014.949616

Carlotti, M. E., Battaglia, L., Ugazio, E., Gallarate, M., & Debernardi, F. (2004). Study on the release properties and stability of o/w emulsions containing salicylic acid and zinc oxide. *Journal of Drug Delivery Science and Technology*, *14*(2), 119–126. https://doi.org/10.1016/s1773-2247(04)50023-0

Chang, C. H., Lin, Y. H., Yeh, C. L., Chen, Y. C., Chiou, S. F., Hsu, Y. M., Chen, Y. S., & Wang, C. C. (2010). Nanoparticles incorporated in pH-sensitive hydrogels as amoxicillin delivery for eradication of Helicobacter pylori. *Biomacromolecules*, *11*(1), 133–142. https://doi.org/10.1021/bm900985h

Choudhary, I. (2020). Effect of excitation wavelength and europium doping on the optical properties of nanoscale zinc oxide. *Journal of Materials Science: Materials in Electronics*, *31*(22), 20033–20042. https://doi.org/10.1007/s10854-020-04525-x

Coates, J. (2006). Interpretation of Infrared Spectra, A Practical Approach. *Encyclopedia of Analytical Chemistry*, 1–23. https://doi.org/10.1002/9780470027318.a5606

Cross, A. J., Leitzmann, M. F., Gail, M. H., Hollenbeck, A. R., Schatzkin, A., & Sinha, R.

(2007). A prospective study of red and processed meat intake in relation to cancer risk. *PLoS Medicine*, *4*(12), 1973–1984. https://doi.org/10.1371/journal.pmed.0040325

Das, S., Das, K., & Dubey, V. (2011). Inhibitory activity and phytochemical assessment of ethno-medicinal plants against some human pathogenic bacteria. *Journal of Medicinal Plant Research*, *5*(29), 6536–6543. https://doi.org/10.5897/jmpr11.777

Devi, P. G., & Velu, A. S. (2016a). Structural , optical and photoluminescence properties of copper and iron doped nanoparticles prepared by co-precipitation method. *Journal of Materials Science: Materials in Electronics*, *27*(10), 10833–10840. https://doi.org/10.1007/s10854-016-5190-1

Devi, P. G., & Velu, A. S. (2016b). Synthesis, structural and optical properties of pure ZnO and Co doped ZnO nanoparticles prepared by the co-precipitation method. *Journal of Theoretical and Applied Physics*, *10*(3), 233–240. https://doi.org/10.1007/s40094-016-0221-0

Emami-karvani, Z., & Chehrazi, P. (2011). *Antibacterial activity of ZnO nanoparticle on gram- positive and gram-negative bacteria*. *5*(12), 1368–1373. https://doi.org/10.5897/AJMR10.159

Fouda, A., EL-Din Hassan, S., Salem, S. S., & Shaheen, T. I. (2018). In-Vitro cytotoxicity, antibacterial, and UV protection properties of the biosynthesized Zinc oxide nanoparticles for medical textile applications. *Microbial Pathogenesis*, *125*, 252–261. https://doi.org/10.1016/j.micpath.2018.09.030

Gadalla, A. A., Abood, I., & Elokr, M. M. (2018). *Structural , Optical and Magnetic Properties of Ni-Doped ZnO Synthesized by Co-Precipitation Method*. *February*. https://doi.org/10.15436/2377-1372.17.1374

Gambichler, T., Avermaete, A., Bader, A., Altmeyer, P., & Hoffmann, K. (2001). Ultraviolet protection by summer textiles. Ultraviolet transmission measurements verified by determination of the minimal erythema dose with solar-simulated radiation. *British Journal of Dermatology*, *144*(3), 484–489. https://doi.org/10.1046/j.1365-2133.2001.04072.x

Gambichler, T., Hatch, K. L., Avermaete, A., Altmeyer, P., & Hoffmann, K. (2002). *in Vitro and in Vivo Measurements*. 29–35.

Gao, X., Zhang, T., Hayden, M., & Roe, C. (2009). Effects of the stress state on plasticity and ductile failure of an aluminum 5083 alloy. *International Journal of Plasticity*, *25*(12), 2366–2382. https://doi.org/10.1016/j.ijplas.2009.03.006

Ghosh, P., & Sharma, A. K. (2013). Optical characterization and growth mechanism of combination of zinc oxide nanowires and nanorods at various substrate temperatures. *Journal of Nanomaterials*, *2013*. https://doi.org/10.1155/2013/480164

Ghrib, T., Massoudi, I., Otaibi, A. L. Al, Al, A., Aya, M., Eman, K., & Hashem, A. (2021). Effects of Terbium Doping on Structural , Optical and Photocatalytic Properties of ZnO Nanopowder Prepared by Solid - State Reaction. *Journal of Inorganic and Organometallic Polymers and Materials,* *31*(1), 239–250. https://doi.org/10.1007/s10904-020-01761-w

Grifoni, D., Bacci, L., Zipoli, G., Carreras, G., Baronti, S., & Sabatini, F. (2009). Laboratory and outdoor assessment of UV protection offered by flax and hemp fabrics dyed with natural dyes. *Photochemistry and Photobiology*, *85*(1), 313–320. https://doi.org/10.1111/j.1751-1097.2008.00439.x

Gunalan, S., Sivaraj, R., & Rajendran, V. (2012). Green synthesized ZnO nanoparticles against bacterial and fungal pathogens. *Progress in Natural Science: Materials International*, *22*(6), 693–700. https://doi.org/10.1016/j.pnsc.2012.11.015

Gunasekaran, S., Sankari, G., & Ponnusamy, S. (2005). Vibrational spectral investigation on xanthine and its derivatives - Theophylline, caffeine and theobromine. *Spectrochimica Acta - Part A: Molecular and Biomolecular Spectroscopy*, *61*(1–2), 117–127. https://doi.org/10.1016/j.saa.2004.03.030

Hahn, Y. (2011). *Zinc oxide nanostructures and their applications*. *28*(9), 1797–1813. https://doi.org/10.1007/s11814-011-0213-3

Hench, L. L., & West, J. K. (1990). The Sol-Gel Process. *Chemical Reviews*, *90*(1), 33–72. https://doi.org/10.1021/cr00099a003

Hoseinzadeh, E., Makhdoumi, P., Taha, P., Hossini, H., Stelling, J., Kamal, M. A., & Ashraf, G. (2017). *REVIEW ARTICLE A Review on Nano-Antimicrobials : Metal Nanoparticles , Methods , and Mechanisms*. 1–9. https://doi.org/10.2174/1389200217666161201111

Hossain, M. A., & Rahman, M. (2015). A Review of Nano Particle Usage on Textile Material against Ultra Violet Radiation. *Journal of Textile Science and Technology*, *01*(03), 93–100. https://doi.org/10.4236/jtst.2015.13010

Iosin, M., Toderas, F., Baldeck, P. L., & Astilean, S. (2009). Study of protein-gold nanoparticle conjugates by fluorescence and surface-enhanced Raman scattering. *Journal of Molecular Structure*, *924–926*(C), 196–200. https://doi.org/10.1016/j.molstruc.2009.02.004

Jamdagni, P., Khatri, P., & Rana, J. S. (2018). Green synthesis of zinc oxide nanoparticles using flower extract of Nyctanthes arbor-tristis and their antifungal activity. *Journal of King Saud University - Science*, *30*(2), 168–175. https://doi.org/10.1016/j.jksus.2016.10.002

Kang, J., Liu, Y., Xie, M. X., Li, S., Jiang, M., & Wang, Y. D. (2004). Interactions of human serum albumin with chlorogenic acid and ferulic acid. *Biochimica et Biophysica Acta - General Subjects*, *1674*(2), 205–214. https://doi.org/10.1016/j.bbagen.2004.06.021

Karakız, M., Altunbas, M., Bacaksiz, E., Parlak, M., Tomakin, M., & Ozc, A. (2008). *The effects of zinc nitrate , zinc acetate and zinc chloride precursors on investigation of structural and optical properties of ZnO thin films*. *466*, 447–450. https://doi.org/10.1016/j.jallcom.2007.11.061

Karthikeyan, C., Arun, L., Hameed, A. S. H., Gopinath, K., Umaralikahan, L., Vijayaprasath, G., & Malathi, P. (2019). Structural, optical, thermal and magnetic properties of nickel calcium and nickel iron co-doped ZnO nanoparticles. *Journal of Materials Science: Materials in Electronics*, *0*(0), 0. https://doi.org/10.1007/s10854-019-01160-z

Kathirvelu, S., D’Souza, L., & Dhurai, B. (2009). UV protection finishing of textiles using ZnO nanoparticles. *Indian Journal of Fibre and Textile Research*, *34*(3), 267–273.

Kolodziejczak-Radzimska, A., & Jesionowski, T. (2014). Zinc oxide-from synthesis to application: A review. *Materials*, *7*(4), 2833–2881. https://doi.org/10.3390/ma7042833

Kumar, P., Singh, B. K., Pal, B. N., & Pandey, P. C. (2016). Correlation between structural, optical and magnetic properties of Mn-doped ZnO. *Applied Physics A: Materials Science and Processing*, *122*(8). https://doi.org/10.1007/s00339-016-0265-7

Liu, B., You, Y., Zhang, H., Wu, H., Jin, J., & Liu, H. (2016). Synthesis of ZnO nano-powders: Via a novel PVA-assisted freeze-drying process. *RSC Advances*, *6*(111), 110349–110355. https://doi.org/10.1039/c6ra24154a

Louris, E., Sfiroera, E., Priniotakis, G., Makris, R., Siemos, H., Efthymiou, C., & Assimakopoulos, M. N. (2018). Evaluating the ultraviolet protection factor (UPF) of various knit fabric structures. *IOP Conference Series: Materials Science and Engineering*, *459*(1), 350. https://doi.org/10.1088/1757-899X/459/1/012051

Lu, J. G., Fan, Z., & Lu, J. G. (2005). *Zinc Oxide Nanostructures : Synthesis and Properties Zinc Oxide Nanostructures : Synthesis and Properties*. *July 2015*. https://doi.org/10.1166/jnn.2005.182

M, S. S., Bose, L., & Kc, G. (2009). *OPTICAL PROPERTIES OF ZnO NANOPARTICLES*. *XVI*(1), 57–65.

Mandal, G., Bhattacharya, S., & Ganguly, T. (2009). Nature of interactions of tryptophan with zinc oxide nanoparticles and l-aspartic acid: A spectroscopic approach. *Chemical Physics Letters*, *472*(1–3), 128–133. https://doi.org/10.1016/j.cplett.2009.03.007

Mishra, A., & Malik, A. (2014). Novel fungal consortium for bioremediation of metals and dyes from mixed waste stream. *Bioresource Technology*, *171*(1), 217–226. https://doi.org/10.1016/j.biortech.2014.08.047

Mishra, S. K., Srivastava, R. K., & Prakash, S. G. (2012). ZnO nanoparticles: Structural, optical and photoconductivity characteristics. *Journal of Alloys and Compounds*, *539*, 1–6. https://doi.org/10.1016/j.jallcom.2012.06.024

Moballegh, A. (2007). *ZnO nanoparticles obtained by mechanochemical technique and the optical properties*. *601*, 2850–2854. https://doi.org/10.1016/j.susc.2006.12.012

Mohamed, A. A., Fouda, A., Abdel-Rahman, M. A., Hassan, S. E. D., El-Gamal, M. S., Salem, S. S., & Shaheen, T. I. (2019). Fungal strain impacts the shape, bioactivity and multifunctional properties of green synthesized zinc oxide nanoparticles. *Biocatalysis and Agricultural Biotechnology*, *19*, 101103. https://doi.org/10.1016/j.bcab.2019.101103

Mohd Omar, F., Abdul Aziz, H., & Stoll, S. (2014). Aggregation and disaggregation of ZnO nanoparticles: influence of pH and adsorption of Suwannee River humic acid. *The*

Science of the Total Environment, *468–469*, 195–201. https://doi.org/10.1016/j.scitotenv.2013.08.044

Morales, F., Cartelat, A., Álvarez-Fernández, A., Moya, I., & Cerovic, Z. G. (2005). Time-resolved spectral studies of blue-green fluorescence of artichoke (Cynara cardunculus L. var. Scolymus) leaves: Identification of chlorogenic acid as one of the major fluorophores and age-mediated changes. *Journal of Agricultural and Food Chemistry*, *53*(25), 9668–9678. https://doi.org/10.1021/jf051842q

Moroni, M., Borrini, D., Calamai, L., & Dei, L. (2005). Ceramic nanomaterials from aqueous and 1,2-ethanediol supersaturated solutions at high temperature. *Journal of Colloid and Interface Science*, *286*(2), 543–550. https://doi.org/10.1016/j.jcis.2005.01.097

Muthukumaran, S., & Gopalakrishnan, R. (2012). Structural, FTIR and photoluminescence studies of Cu doped ZnO nanopowders by co-precipitation method. *Optical Materials*, *34*(11), 1946–1953. https://doi.org/10.1016/j.optmat.2012.06.004

Newman, M. D., Stotland, M., & Ellis, J. I. (2009). The safety of nanosized particles in titanium dioxide- and zinc oxide-based sunscreens. *Journal of the American Academy of Dermatology*, *61*(4), 685–692. https://doi.org/10.1016/j.jaad.2009.02.051

Ntwaeaborwa, O. M., Mofokeng, S. J., Kumar, V., & Kroon, R. E. (2017). Structural, optical and photoluminescence properties of Eu3 + doped ZnO nanoparticles. *Spectrochimica Acta - Part A: Molecular and Biomolecular Spectroscopy*, *182*, 42–49. https://doi.org/10.1016/j.saa.2017.03.067

Özgür, Ü., Alivov, Y. I., Liu, C., Teke, A., Reshchikov, M. A., Doğan, S., Avrutin, V., Cho, S. J., & Morkọ, H. (2005). A comprehensive review of ZnO materials and devices. *Journal of Applied Physics*, *98*(4), 1–103. https://doi.org/10.1063/1.1992666

Parihar, V., Raja, M., & Paulose, R. (2018). *A BRIEF REVIEW OF STRUCTURAL , ELECTRICAL AND ELECTROCHEMICAL PROPERTIES OF ZINC OXIDE NANOPARTICLES*.

Parra, M. R., & Haque, F. Z. (2014). Aqueous chemical route synthesis and the effect of calcination temperature on the structural and optical properties of ZnO nanoparticles. *Journal of Materials Research and Technology*, *3*(4), 363–369. https://doi.org/10.1016/j.jmrt.2014.07.001

Pérez-Maqueda, L. A., Wang, L., & Matijević, E. (1998). Nanosize indium hydroxide by peptization of colloidal precipitates. *Langmuir*, *14*(16), 4397–4401. https://doi.org/10.1021/la980149c

Phuruangrat, A., Yayapao, O., Thongtem, T., & Thongtem, S. (2014). *Synthesis and Characterization of Europium-Doped Zinc Oxide Photocatalyst*. *2014*.

Pradeev, K., Sadaiyandi, K., Kennedy, A., Sagadevan, S., Chowdhury, Z. Z., Rafie, M., Johan, B., Aziz, F. A., Rafique, R. F., Selvi, R. T., & Rathina, R. (2018). *Influence of Mg Doping on ZnO Nanoparticles for Enhanced Photocatalytic Evaluation and Antibacterial Analysis*.

Pradeev Raj, K., Sadaiyandi, K., Kennedy, A., & Sagadevan, S. (2017). Photocatalytic and antibacterial studies of indium-doped ZnO nanoparticles synthesized by co-precipitation technique. *Journal of Materials Science: Materials in Electronics*, *28*(24), 19025–19037. https://doi.org/10.1007/s10854-017-7857-7

Preethi, S., Anitha, A., & Arulmozhi, M. (2016). A comparative analysis of the properties of zinc oxide (ZnO) nanoparticles synthesized by hydrothermal and sol-gel methods. *Indian Journal of Science and Technology*, *9*(40), 1–6. https://doi.org/10.17485/ijst/2016/v9i40/92696

Raj, K. P., Sadaiyandi, K., Kennedy, A., & Thamizselvi, R. (2016). Structural , optical , photoluminescence and photocatalytic assessment of Sr-doped ZnO nanoparticles. *Materials Chemistry and Physics*, *183*, 24–36. https://doi.org/10.1016/j.matchemphys.2016.07.068

Raji, R., & Gopchandran, K. G. (2017). ZnO nanostructures with tunable visible luminescence: Effects of kinetics of chemical reduction and annealing. *Journal of Science: Advanced Materials and Devices*, *2*(1), 51–58. https://doi.org/10.1016/j.jsamd.2017.02.002

Raoufi, D. (2013). Synthesis and microstructural properties of ZnO nanoparticles prepared by precipitation method. *Renewable Energy*, *50*, 932–937. https://doi.org/10.1016/j.renene.2012.08.076

Riva, A., Algaba, I. M., & Pepió, M. (2006). Action of a finishing product in the improvement of the ultraviolet protection provided by cotton fabrics. Modelisation of the effect. *Cellulose*, *13*(6), 697–704. https://doi.org/10.1007/s10570-006-9085-9

Rl, M., Kv, U., & Naik, D. (2019). *Synthesis and characterization of ZnO nanoparticles : A review*. *8*(3), 1095–1101.

Ross, P. D., & Subramanian, S. (1981). Thermodynamics of Protein Association Reactions: Forces Contributing to Stability. *Biochemistry*, *20*(11), 3096–3102. https://doi.org/10.1021/bi00514a017

S, G., Belay, A., Reddy AR, C., & Z, B. (2017). Synthesis and Characterizations of Zinc Oxide Nanoparticles for Antibacterial Applications. *Journal of Nanomedicine & Nanotechnology*, *s8*(June). https://doi.org/10.4172/2157-7439.s8-004

Sa-nguanprang, S., Phuruangrat, A., Thongtem, T., & Thongtem, S. (2019). Synthesis, Analysis, and Photocatalysis of Mg-Doped ZnO Nanoparticles. *Russian Journal of Inorganic Chemistry*, *64*(14), 1841–1848. https://doi.org/10.1134/S0036023619140158

Salahuddin, N. A., El-kemary, M., & Ibrahim, E. M. (2015). *Synthesis and Characterization of ZnO Nanoparticles via Precipitation Method : Effect of Annealing Temperature on Particle Size*. *5*(4), 82–88. https://doi.org/10.5923/j.nn.20150504.02

Sawai, J. (2003). Quantitative evaluation of antibacterial activities of metallic oxide powders (ZnO, MgO and CaO) by conductimetric assay. *Journal of Microbiological Methods*, *54*(2), 177–182. https://doi.org/10.1016/S0167-7012(03)00037-X

Sawhney, A. P. S., Condon, B., Singh, K. V., Pang, S. S., li, G., & Hui, D. (2008). Modern Applications of Nanotechnology in Textiles. *Textile Research Journal*, *78*(8), 731–739. https://doi.org/10.1177/0040517508091066

Shateri-Khalilabad, M., & Yazdanshenas, M. E. (2013). Bifunctionalization of cotton textiles by ZnO nanostructures: Antimicrobial activity and ultraviolet protection. *Textile Research Journal*, *83*(10), 993–1004. https://doi.org/10.1177/0040517512468812

Siddiqi, K. S., Rahman, A., & Husen, A. (2018). *Properties of Zinc Oxide Nanoparticles and Their Activity Against Microbes*.

Singh, R. G., Singh, F., Kumar, V., & Mehra, R. M. (2011). Growth kinetics of ZnO nanocrystallites: Structural, optical and photoluminescence properties tuned by thermal annealing. *Current Applied Physics*, *11*(3), 624–630.

https://doi.org/10.1016/j.cap.2010.10.013

Sirelkhatim, A., Mahmud, S., & Seeni, A. (2015). Review on Zinc Oxide Nanoparticles : Antibacterial Activity and Toxicity Mechanism. *Nano-Micro Letters, 7,* 219–242. https://doi.org/10.1007/s40820-015-0040-x

Stefaniuk, I., Cieniek, B., Rogalska, I., Virt, I. S., & Kosciak, A. (2018). Magnetic properties of ZnO:Co layers obtained by pulsed laser deposition method. *Materials Science-Poland, 36*(3), 439–444. https://doi.org/10.1515/msp-2017-0114

Talam, S., Karumuri, S. R., & Gunnam, N. (2012). Synthesis, Characterization, and Spectroscopic Properties of ZnO Nanoparticles. *ISRN Nanotechnology, 2012*, 1–6. https://doi.org/10.5402/2012/372505

Uddin, M. J., Cesano, F., Scarano, D., Bonino, F., Agostini, G., Spoto, G., Bordiga, S., & Zecchina, A. (2008). Cotton textile fibres coated by Au/TiO2 films: Synthesis, characterization and self cleaning properties. *Journal of Photochemistry and Photobiology A: Chemistry*, *199*(1), 64–72. https://doi.org/10.1016/j.jphotochem.2008.05.004

Upadhyaya, H., Shome, S., Sarma, R., & Tewari, S. (2018). *Green Synthesis , Characterization and Antibacterial Activity of ZnO Nanoparticles*. 1279–1291. https://doi.org/10.4236/ajps.2018.96094

Vigneshwaran, N., Kumar, S., Kathe, A. A., Varadarajan, P. V., & Prasad, V. (2006). Functional finishing of cotton fabrics using zinc oxide-soluble starch nanocomposites. *Nanotechnology, 17*(20), 5087–5095. https://doi.org/10.1088/0957-4484/17/20/008

Vijayaprasath, G., Murugan, R., Asaithambi, S., Babu, G. A., Sakthivel, P., Mahalingam, T., Hayakawa, Y., & Ravi, G. (2016). Structural characterization and magnetic properties of Co co-doped Ni/ZnO nanoparticles. *Applied Physics A: Materials Science and Processing, 122*(2), 1–11. https://doi.org/10.1007/s00339-016-9655-0

Vijayaprasath, G., Soundarrajan, P., & Ravi, G. (2018). The point defects induced ferromagnetism in ZnO semiconductor by terbium doping via co-precipitation method. *Journal of Materials Science: Materials in Electronics*, *29*(14), 11892–11900. https://doi.org/10.1007/s10854-018-9290-y

Wang, Y., Zhang, C., Bi, S., & Luo, G. (2010). Preparation of ZnO nanoparticles using the direct precipitation method in a membrane dispersion micro-structured reactor. *Powder Technology*, *202*(1–3), 130–136. https://doi.org/10.1016/j.powtec.2010.04.027

Wang, Z. L. (2004). *Zinc oxide nanostructures : growth , properties and applications applications*. https://doi.org/10.1088/0953-8984/16/25/R01

Xin, J. H., Daoud, W. A., & Kong, Y. Y. (2004). A New Approach to UV-Blocking Treatment for Cotton Fabrics. *Textile Research Journal*, *74*(2), 97–100. https://doi.org/10.1177/004051750407400202

Yuvakkumar, R., Suresh, J., Nathanael, A. J., Sundrarajan, M., & Hong, S. I. (2014). Novel green synthetic strategy to prepare ZnO nanocrystals using rambutan (Nephelium lappaceum L.) peel extract and its antibacterial applications. *Materials Science and Engineering C*, *41*, 17–27. https://doi.org/10.1016/j.msec.2014.04.025

Zarrindokht Emami-Karvani. (2012). Antibacterial activity of ZnO nanoparticle on Gram-positive and Gram-negative bacteria. *African Journal of Microbiology Research*, *5*(18). https://doi.org/10.5897/ajmr10.159

Zhang, J. (2011). Silver-coated zinc oxide nanoantibacterial synthesis and antibacterial activity characterization. *ICEOE 2011 - 2011 International Conference on Electronics and Optoelectronics, Proceedings*, *3*(Iceoe), 94–98. https://doi.org/10.1109/ICEOE.2011.6013309

Zhang, L., Jiang, Y., Ding, Y., Povey, M., & York, D. (2007). Investigation into the antibacterial behaviour of suspensions of ZnO nanoparticles (ZnO nanofluids). *Journal of Nanoparticle Research*, *9*(3), 479–489. https://doi.org/10.1007/s11051-006-9150-1

Zhong, Q., & Matijević, E. (1996). Preparation of uniform zinc oxide colloids by controlled double-jet precipitation. *Journal of Materials Chemistry*, *6*(3), 443–447. https://doi.org/10.1039/jm9960600443